



OPEN Cdk5 mediates rotational force-induced brain injury

Alan Umfress¹, Ayanabha Chakraborti², Suma Priya Sudarsana Devi¹, Raegan Adams¹, Daniel Epstein¹, Adriana Massicano³, Anna Sorace³, Sarbjit Singh⁴, M. Iqbal Hossain⁵, Shaida A. Andrabi⁵, David K. Crossman⁶, Nilesh Kumar⁷, M. Shahid Mukhtar^{4,7}, Huiyang Luo⁸, Claire Simpson⁹, Kathryn Abell⁹, Matthew Stokes⁹, Thorsten Wiederhold⁹, Charles Rosen¹⁰, Hongbing Lu¹¹, Amarnath Natarajan⁴ & James A. Bibb²✉

Millions of traumatic brain injuries (TBIs) occur annually. TBIs commonly result from falls, traffic accidents, and sports-related injuries, all of which involve rotational acceleration/deceleration of the brain. During these injuries, the brain endures a multitude of primary insults including compression of brain tissue, damaged vasculature, and diffuse axonal injury. All of these deleterious effects can contribute to secondary brain ischemia, cellular death, and neuroinflammation that progress for weeks, months, and lifetime after injury. While the linear effects of head trauma have been extensively modeled, less is known about how rotational injuries mediate neuronal damage following injury. Here, we developed a new model of repetitive rotational head trauma in rodents and demonstrated acute and prolonged pathological, behavioral, and electrophysiological effects of rotational TBI (rTBI). We identify aberrant Cyclin-dependent kinase 5 (Cdk5) activity as a principal mediator of rTBI. We utilized Cdk5-enriched phosphoproteomics to uncover potential downstream mediators of rTBI and show pharmacological inhibition of Cdk5 reduces the cognitive and pathological consequences of injury. These studies contribute meaningfully to our understanding of the mechanisms of rTBI and how they may be effectively treated.

Traumatic brain injuries occur in epidemic proportions with over 1.5 million injuries occurring annually in the United States alone¹. During a TBI, the brain undergoes both linear and rotational forces, compressing tissue and damaging axonal connections. While the linear effects of injury primarily result in focal brain damage, rotational acceleration of the brain produces shearing forces resulting in both focal and diffuse neuropathology. Diffuse axonal shearing as the result of rotational TBI (rTBI) causes persistent neuropathological consequences of brain trauma^{2–4}. At the time of injury, rapid brain acceleration/deceleration creates a disruption of brain tissue resulting in contusion, blood vessel damage, hemorrhage, and axonal shearing⁵. TBI results in acute dysfunctions in cognition including loss of consciousness, headaches, and vision problems⁶. Secondary damage evolves over the following days, months, and lifetime of survivors leading to impairments in memory and motor function, anxiety disorders, and neurodegeneration^{7–10}.

At cellular resolution, rTBI induces axonal shearing resulting in massive neuronal depolarization and ionic influx^{11–15}. In response, activation of voltage gated Ca²⁺ channels induce excitotoxic release of glutamate. Following excitotoxicity, cerebral edema, oxidative stress, and cellular death all contribute to the acute phase of injury^{1,16,17}. After initial trauma, a delayed spreading process of injury occurs. The injured brain exhibits increased sensitivity to secondary ischemic insult and persistent excitotoxicity¹⁸. Secondary damage advances over weeks, months, and years after injury, impairing neurological function and impeding recovery¹⁹. Chronic effects from TBI include increased risk of developing Alzheimer's disease (AD), increased risk of developing Parkinson's disease (PD), and neurodegeneration in the form of chronic traumatic encephalopathy (CTE)^{20–22}.

¹Department of Surgery, University of Alabama at Birmingham, Birmingham, AL, USA. ²Department of Translational Neuroscience, University of Arizona College of Medicine in Phoenix, Biomedical Sciences Partnership Bldg, Phoenix, AZ 85004, USA. ³Department of Radiology, University of Alabama at Birmingham, Birmingham, AL, USA. ⁴Eppley Institute for Research in Cancer and Allied Diseases University of Nebraska Medical Center, Omaha, NE, USA. ⁵Department of Pharmacology and Toxicology, University of Alabama at Birmingham, Birmingham, AL, USA. ⁶Department of Genetics, University of Alabama at Birmingham, Birmingham, AL, USA. ⁷Department of Biology, University of Alabama at Birmingham, Birmingham, AL, USA. ⁸Karagozian & Case, Inc., Glendale, CA, USA. ⁹Cell Signaling Technology, Danvers, MA, USA. ¹⁰OSF Healthcare Illinois Neurological Institute, Peoria, IL, USA. ¹¹Department of Mechanical Engineering, University of Texas at Dallas, Dallas, TX, USA. ✉email: jbibb@arizona.edu

The disruption of intracellular signaling cascades serves as a convergence point of ischemia, inflammation, and excitotoxicity where the activation of downstream effectors induces cellular demise. One such excitotoxic pathway is the dysregulation of the protein kinase cyclin dependent kinase 5 (Cdk5) via the calpain family of Ca^{2+} -activated neutral proteases²³. Following cellular damage, activated calpain protease cleaves the coactivator of Cdk5, p35, into a truncated aberrant coactivator, p25²⁴. Conversion of Cdk5/p35 to Cdk5/p25 by calpain confers neurotoxic activity upon the kinase, resulting in neuronal injury and death²⁵. Aberrant Cdk5/p25 contributes to virtually all neurodegenerative diseases and is key to the general processes by which neurotoxicity occurs^{25–27}. Conditional knockout of Cdk5 confers neuroprotection from cortical impact, ischemic stroke, and mouse models of AD^{23,28,29}. Therefore, we hypothesized that aberrant Cdk5/p25 activity may mediate the neuropathological and neurocognitive effects of repeated and rotational brain injuries. To test this, we designed and characterized a novel model of rTBI and assessed the neuropathological effects of repetitive injury in the acute and subacute phases, including aberrant Cdk5/p25 activation. We assessed a new systemic Cdk5 inhibitor (25–106) as a potential treatment for rTBI. Finally, we conducted Cdk5-enriched phosphoproteomics to identify novel downstream effectors of brain injury. Together, these studies provide a better understanding of the mechanisms mediating injury by rTBI and point to a potentially effective therapeutic approach.

Results

Development and characterization of a rotational traumatic brain injury (rTBI) model in rats.

To assess the negative consequences of rotational head injury, we developed a novel repetitive rTBI model with the ability to impart clinically relevant angular accelerations (Fig. 1A). The model consists of a pneumatic-chain driven pendulum arm attached to an animal carrier. This pendulum rotates about a horizontal shaft. The rodent is placed in a restraint inserted onto a fixed mount at the end of the pendulum (Fig. 1A, B) and attached to the freely rotating helmet assembly bolted to the restraint mount (Fig. 1C), allowing pure coronal plane head rotation. A ventral strike plate (Fig. 1D) transfers impact momentum between the harness and impact fixture, imparting rotational force on the subject's head. The pendulum is rapidly propelled forward using a compressed N_2 -driven 2-way solenoid valve (Fig. 1E, F) that subsequently drives an air motor inducing rapid chain rotation. Accelerometry is derived from a helmet mounted inertial measurement unit (IMU) model 633, a 6-degrees of freedom transducer incorporating accelerometers and gyroscopes comprised of micro-machined silicon sensors (Fig. 1G, H). IMU data is captured in LabVIEW and converted to acceleration measured in gravitational constants (g values), which are converted to angular acceleration (rad/sec^2).

To validate helmet sensor accelerometry, we utilized high speed video telemetry to determine angular speed of the helmet and compared these values to those derived from the helmet sensor (Fig. 1I–L). Video telemetry and helmet sensor showed highly overlapping determinates for angular speed. Typical machine runs induce average helmet peak rotational acceleration outputs averaging $482\text{Krad}/\text{s}^2$ with limited variability across 5 sampling runs of $14.15\text{Krad}/\text{s}^2$ (Fig. 1M). These angular accelerations are consistent with human to animal scaling laws for mild brain injuries^{30,31}, suggesting rTBI studies using this model in rodents may readily translate to human conditions.

Neuropathological consequences of rTBI. The consequences of rTBI include acute and prolonged pathological alterations including damaged vasculature, diffuse axonal injury, inflammation, cellular demise, and neurodegeneration⁵. To investigate the effects of rTBI, we first conducted PET/CT neuropathology studies. For these studies, we made use of a diagnostic molecular probe in current clinical use for the detection of the neuroinflammatory marker, translocator protein (TSPO). This probe, [^{18}F]DPA-714 detects activated microglia resulting from neuroinflammation in neurodegenerative and neuroinflammatory conditions^{32–34}. TSPO imaging revealed differential uptake diffusely throughout the brains of both control and rTBI rats 7 days post-injury (Fig. 2A). Interestingly, standard uptake values (SUV) were significantly increased in several brain regions including amygdala, hippocampus CA1 layer, and the basolateral amygdaloid nucleus of rTBI rats 7 days post-injury in comparison to controls (Fig. 2B–D). Effects were also observed diffusely throughout whole cortex with cortical areas including perirhinal and primary somatosensory cortex showing higher labeling following rTBI (Supplemental Fig. 1A–C). The differential labeling was region-specific as no effect was detectable when signal throughout whole brain was quantitated (Supplemental Fig. 1D). Also, regions such as hippocampus layer CA3 and cerebellum exhibited no change in response to impact (Supplemental Fig. 1E, F). Thus, rTBI caused brain region-specific alterations in this biomarker of neuroinflammation, consistent with effects observed in humans³².

In addition to *in vivo* imaging, immunostaining was used to assess neuroinflammatory effects of rTBI. For these experiments, layers of the hippocampal formation were examined, as rTBI effects within this brain region in humans have been linked to consequent memory impairments^{35–37}. Indeed, broad increases in microgliosis were detected throughout the CA1 subfield of the hippocampus (Fig. 2E) 48 h post-injury. Furthermore, rats subjected to rTBI showed increased astrogliosis throughout the CA1 (Fig. 2F). Chronic consequences of brain injury include tauopathy occurring in CTE³⁸. To assess chronic neuropathological changes following rTBI, rats 6 months post injury were assessed for increased phospho-Tau (AT8) immunoreactivity. Remarkably, rotational injury induced an increase in AT8 immunoreactivity throughout the brain at 6 months post-injury particularly in areas surrounding vasculature (Fig. 2G, Top). We also observed increased AT8 staining, with diffuse staining throughout the neuropil in regions of the CA1 in rTBI rats as compared to age-matched controls (Fig. 2G, Bottom). Another pathological hallmark of TBI is axonal injury³⁹. To assess any structural damage to axons of the hippocampus, we stained the CA1 subregion for phosphorylated neurofilaments (SMI-31), a marker of axonal injury⁴⁰. We observed an increased in SMI-31 48 h after injury, but not 14 days after rTBI (Fig. 2H). Together, these *in vivo* imaging and histological studies demonstrate rotational head injury induces neuroinflammation and axonal damage in acute and sub-acute phases of injury. These effects underlie prolonged changes in AT8 immunoreactivity.

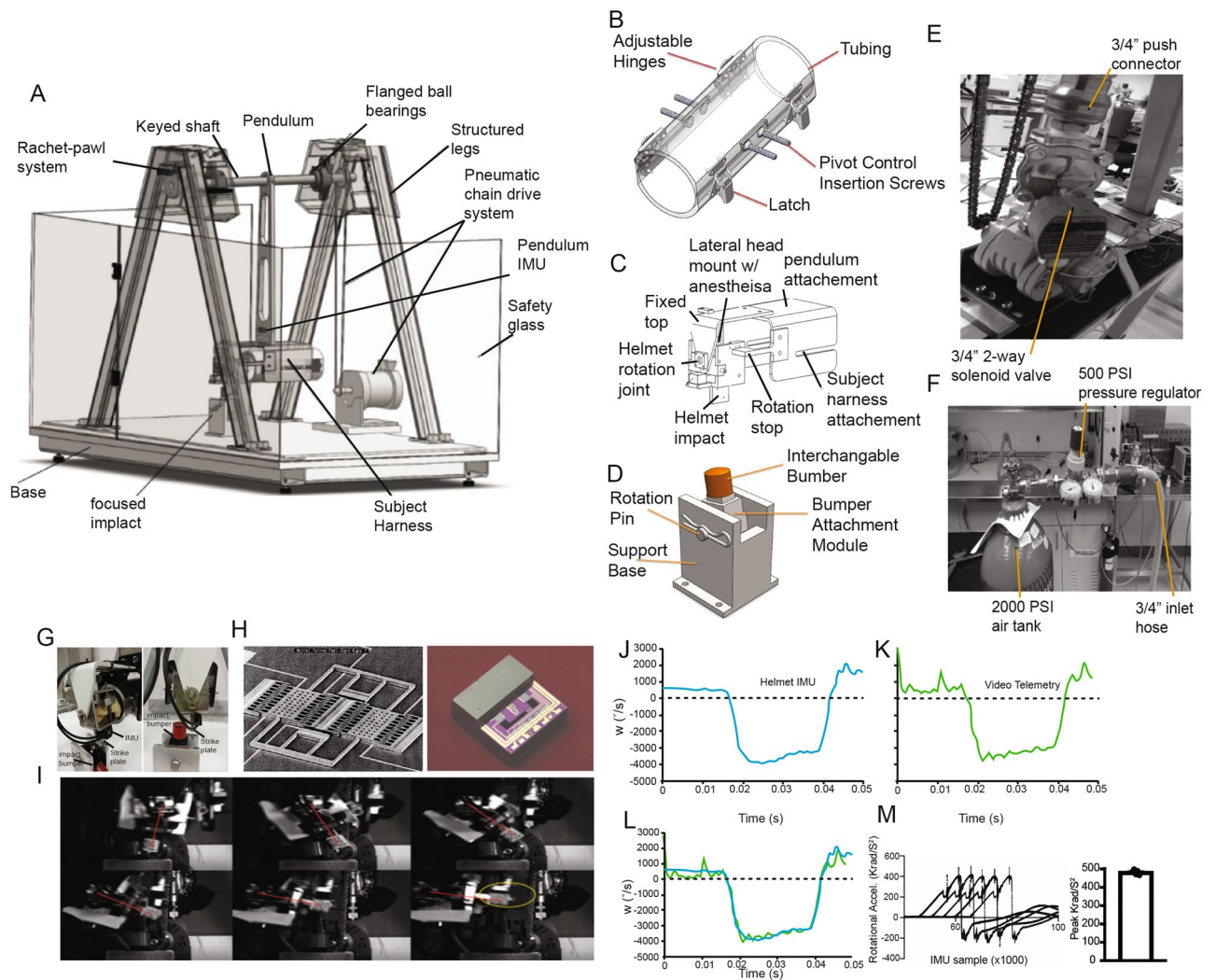


Figure 1. Novel rodent model of rotational traumatic brain injury (rTBI). (A) Rotational head injury model, components, and complete design. (B) Animal restraint. (C) Helmet and subject constraint mount. (D) Ventral strike plate. E. Pneumatic-chain drive system. (F) Pneumatic pressure system. (G) Side view of helmet assembly and restraint with artificial rat. Note model 633 IMU mounted on helmet strike plate below rat head with front view showing strike plate and impact bumper. (H) Model 633 6DOF inertia measurement unit. Oscillating variable capacitance gyro sensor combs (right) and half cover removed view of IMU showing acceleration sensor, mass, supports, and circuitry. (I) Temporally sequential high-speed camera recording frames used to derive acceleration rates. (J) Sample recording from IMU. (K) Video telemetry calculated rate vs. time. (L) Overlay of helmet IMU and video telemetry angular speeds ($^{\circ}/s$) as a function of time. (M) Labview derived rotational accelerations ($Krad/S^2$) of 5 trial runs (left). Peak rotational accelerations for each run with standard error (right).

Behavioral and neurophysiological consequences of rTBI. Persistent memory impairment is a common outcome following TBI⁸. Patients report symptoms including both anterograde and retrograde amnesia, as well as cognitive deficits in attention, processing speed, and executive functioning⁴¹. These deficits often correlate with structural damage to temporal brain areas³⁵ and damage within the hippocampal formation following TBI can contribute to long-lasting deficits in memory⁴². Therefore, we investigated the functional and physiological consequences of rTBI on hippocampal-dependent memory and plasticity in our model. To assess effects on contextual and cued fear learning and memory, rats (7 days post-injury) were placed in a novel context, analyzed for baseline freezing responses, and subsequently exposed to fear conditioning cue/foot shock pairings for assessment of learning and memory function (Fig. 3A). Rats subjected to rTBI displayed no alteration in baseline freezing rates. However, rTBI rats showed a marked decrease in freezing behavior in response to re-exposure to the adverse context. Additionally, rTBI rats displayed a reduction in cue-induced freezing rates in a novel context, suggesting that both hippocampal- and amygdala-mediated components of this learned behavior were impaired. This reduction in freezing responses was not confounded by injury-induced damage to nociceptive circuitry, as shock stimulus pain thresholds for animal flinching, jumping, and vocalizing pain were

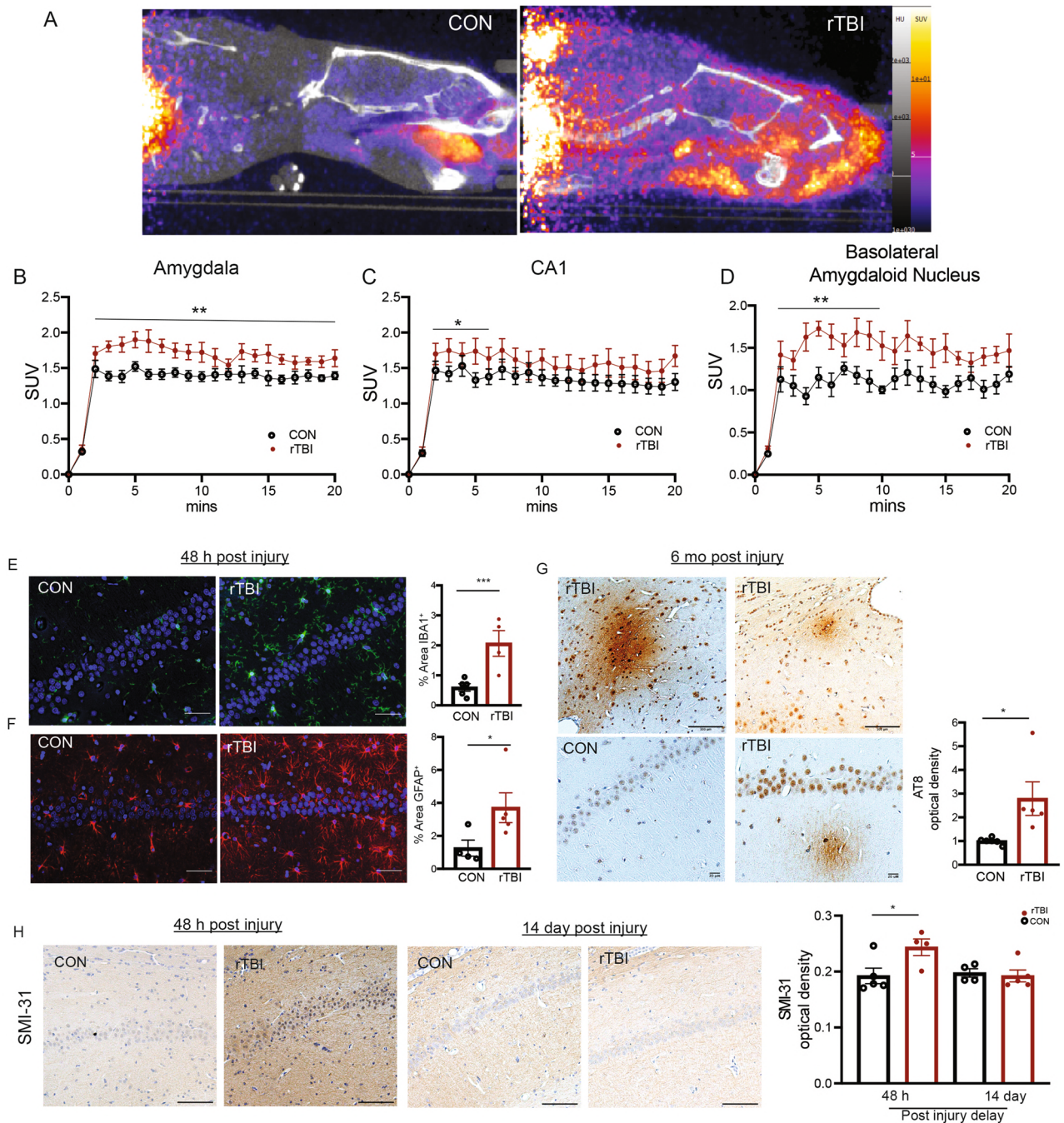


Figure 2. Neuropathological effects of rTBI. **(A)** Representative PET/CT images for TSPO uptake in control (left) and rTBI (right) rats ($n=6$ per group). **(B)** Quantitative Standard uptake values (SUV) for TSPO radioligand in amygdala (Time: $F(20,200) = 110.6$, $p < 0.0001$; Treatment: $F(1, 10) = 7.771$, $p = 0.0192$; Interaction: $F(20, 200) = 2.321$, $p = 0.0017$) two-way-RM ANOVA. **(C)** CA1 (Time: $F(5,50) = 216.4$, $p < 0.0001$; Treatment: $F(1,10) = 1.711$, $p = 0.2202$; Interaction: $F(5,50) = 2.614$, $p = 0.0355$) two-way-RM ANOVA. **(D)** Basolateral amygdaloid nucleus (Time: $F(10,100) = 49.67$, $p < 0.0001$; Treatment: $F(1,10) = 13.97$, $p = 0.0039$; Interaction: $F(10,100) = 2.605$, $p = 0.0075$). **(E)** Histological staining and quantitation for IBA1⁺ microglia within CA1, $p = 0.0083$ Student's *t*-test. ($n = 4-5$ per group) Scale bars = 50 μm . **(F)** Histological staining and quantitation for GFAP⁺ astrocytes within CA1, $p = 0.0317$ Mann Whitney test ($p = 0.0300$, Shapiro-Wilk) ($n = 4-5$ per group) Scale bars = 50 μm . **(G)** Histological staining for AT8⁺ (Top, left) and condensed staining around vessels (Top, right) Scale bars = 100 μm . Histological staining and quantification of AT8 density in CA1 at 6 months post injury (bottom) $p = 0.0210$ Student's *t*-test ($n = 5$ per group) Scale bars = 20 μm . **(H)** Histological staining for SMI-31 at 48 h and 14 days post injury. ($n = 4-5$ per group) (48 h Con-TBI, $p = 0.0409$ Student's *t*-test). All data are means \pm SEM, * $p < 0.05$, ** $p < 0.01$, *** $p < 0.001$, **** $p < 0.0001$.

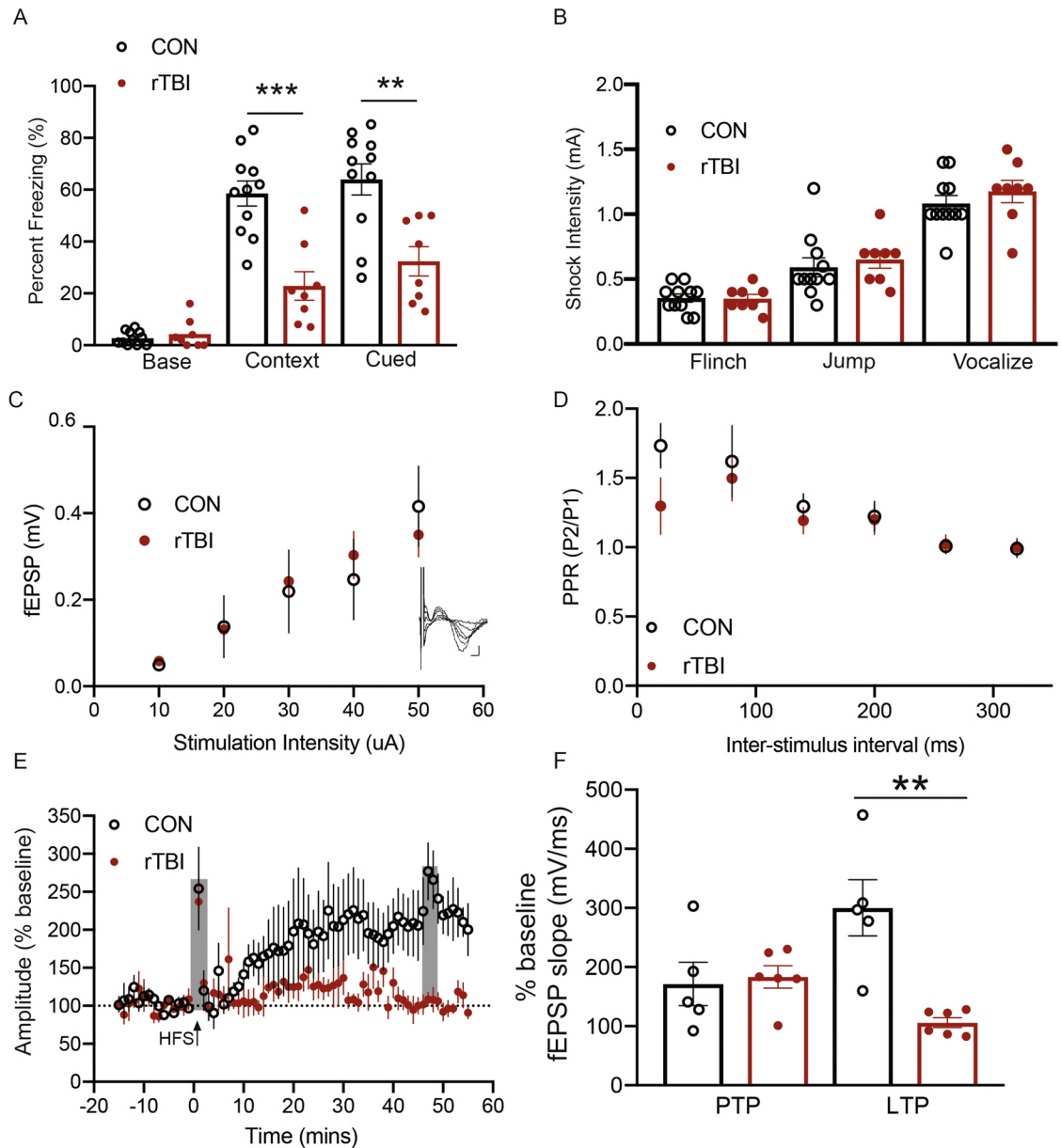


Figure 3. Behavioral and neurophysiological consequences of rTBI. **(A)** Fear conditioning freezing rates for baseline, Contextual, $p=0.0001$ Student's t -test, and Cued, $p=0.0018$ Student's t -test fear learning ($n=8-11$ per group). **(B)** Shock sensitivity thresholds to flinch, jump, or vocalize pain ($n=8-11$ per group). **(C)** Input-Output curve of CA3-CA1 fEPSP recordings (Inset: individual traces for each of the stimulus intensities) ($n=5-6$ per group). **(D)** Paired Pulse Ratio (PPR) across inter-stimulus interval ($n=5-6$ per group). **(E)** Assessment of the effect of rTBI on hippocampal plasticity after HFS ($n=5-6$ per group). (PTP outlined grey 0–2 min, LTP outlined grey 45–55 min). **(F)** Summary of PTP and LTP fEPSP slopes, ($n=5-6$ per group) $p=0.7662$, PTP; $p=0.0017$, LTP Student's t -test. All data are means \pm SEM, * $p < 0.05$, ** $p < 0.01$, *** $p < 0.001$.

not altered by rTBI (Fig. 3B). Thus, rTBI caused learning and memory deficits that persisting into the sub-acute phase of injury.

The observed mnemonic impairments in response to rTBI suggest that hippocampal circuitry function may be damaged. To investigate this possibility, field excitatory post synaptic potential (fEPSP) recordings were taken from hippocampal CA3-CA1 circuitry (7 days post-injury) (Fig. 3C–F). Synaptic excitability, as assessed via stimulus-to-fEPSP amplitude ratios (I/V curves), was unaffected by rTBI (Fig. 3C). The paired-pulse ratio paradigm was used to assess changes on neurotransmitter release. Similarly, this metric of short-term plasticity remained unaltered in rTBI rats (Fig. 3D). Additionally, high frequency stimulation (HFS) induced a $171.4 \pm 36\%$ post-tetanic potentiation (PTP) in control rats compared to baseline (Fig. 3E, F). This effect was similar ($183.4 \pm 18\%$) in rTBI brains. HFS also induced robust ($300 \pm 47\%$) long-term potentiation (LTP) of fEPSP slope compared to baseline 45 min post-stimulus at Schaffer collateral-CA1 synapses of control mice. (Fig. 3E,

F). In contrast, tetanic stimulation caused a markedly smaller effect ($106 \pm 8\%$) in rTBI rats, almost completely ablating the ability to induce LTP. Thus, rTBI caused a notable impairment in hippocampal long-term synaptic plasticity as a likely mechanism underlying the deficit it induced in learning and memory.

Proteomic alterations following rTBI. TBI may impart long-lasting impairments through alterations in protein expression that lead to cell death or inflammatory pathways ultimately leading to neuronal demise. To ascertain the effects of rTBI on protein levels as a net measure of the balance between expression and degradation, we conducted global proteomics to identify mechanisms of rTBI associated with the acute inflammatory state of the hippocampus we observed at 48 h post-injury (Fig. 4A). We noted 234 proteins demonstrated increased expression ($FC \geq 1.3$) and 250 proteins with decreased expression ($FC \leq -1.3$) (Fig. 4B) in rTBI hippocampus relative to controls. The altered expression observed in the proteomic analysis within rTBI lysates was independently validated for two specific proteins (Supplemental Fig. 2A, B). Proteomic analysis revealed animals subjected to rTBI displayed a 1.6 FC of Legumain (LGMN) protease following injury (Fig. 4B). Immunoblot analysis of hippocampal lysates confirmed LGMN is significantly upregulated in expression following injury (Supplemental Fig. 2A). Additionally, Epoxide hydroxylase 2 (EPHX2) displayed a FC increase of 3.9 in rTBI rats compared to control rats. Similarly, immunoblot analysis displayed significant increases of EPHX2 in hippocampal lysates following injury (Supplemental Fig. 2B).

To identify the intracellular pathways altered via rTBI we conducted ingenuity pathways analysis of the top upregulated and downregulated proteins following rTBI (Fig. 4C). Interestingly, rTBI induced upregulation of known cell death dependent pathways linked to brain injury such as ferroptosis and phagosome formation^{43,44}. We observed bidirectional alterations in homeostatic signaling pathways such as Protein Kinase A (PKA) and oxytocin signaling pathways, both of which have been observed to mediate injury in stroke and TBI^{45,46}.

Downregulated pathways after injury included proteins associated with inflammatory response elements such as acute phase response signaling were downregulated in the hippocampus following rTBI. Notably, neurotropic signaling such as those involving neuregulin and wound healing pathways were also downregulated following rTBI. Utilizing an open-source single-cell gene expression atlas of the mouse brain, we determined the cell-type expression profiles of key upregulated proteins following rTBI⁴⁷ (Fig. 4D). Differentially expressed following rTBI displayed cell-type specific alterations in numerous cell-types within immune cell classes such as microglia (MG), neutrophils (NEUT), dendritic cells (DC), macrophages (MAC), and monocytes (MNC). Proteomic expression was also altered in many vascular cell lineages such as endothelial cells (EC), vascular smooth muscle cells (VSMC), arachnoid barrier cells (ABC), and vascular and leptomeningeal cells (VLMC). Interestingly, we noted of the top differentially expressed proteins assessed, they showed limited or no expression in cell-types of astrocyte lineage such as astrocytes (ASC) and astrocyte restricted precursors (ARP). Likewise, limited proteomic alterations were observed in mature (NEUR_mature), immature (NEUR_immature) and neuroendocrine (NendC) neuronal cell lineages. These data likely indicate global proteomic expression changes are occurring in response to inflammatory immune states and damaged vasculature following rTBI. Altogether, these analyses reveal protein expression changes that may mediate aspects of rTBI and highlight cell types and pathways linked to inflammatory responses which may ultimately contribute to the consequences of injury.

rTBI and excitotoxicity evoke aberrant Cdk5 activity and Cdk5 inhibition is neuroprotective. Inflammation due to injury induces excitotoxic states within surrounding neurons, impairing neuronal physiology, neuronal signaling, and ultimately contributing to impaired behavior⁴⁸. TBI-induced excitotoxicity triggers loss of Ca^{2+} homeostasis subsequently leading to the activation of calpain proteases and neuronal demise⁴⁹. A prime target for calpain in neuronal death is the Cdk5 cofactor p35. The activation of calpain and consequent truncation of the Cdk5 coactivator p35 to its aberrant coactivator p25²⁴. The Cdk5/p25 complex has been implicated in various forms of neuronal injury including ischemic stroke, cortical impact, and blast TBI^{23,28,50}. Generation of the aberrantly active Cdk5/p25 complex is neurotoxic⁵¹. Cdk5/p25 hyperphosphorylates Tau in models of AD and causes neuronal cell death⁵². Thus, aberrant Cdk5 invoked by excitotoxicity is a common neuronal injury mechanism shared by many neuropathological conditions^{28,53}.

To better understand the role of aberrant Cdk5 in mediating excitotoxicity in rTBI, we first treated ex vivo brain slices with high concentrations of NMDA (100 μ M) and glycine (gly) (50 μ M) to induce excitotoxicity. This treatment caused significant generation of p25 (Fig. 5A). While over-expression of p25 is neurotoxic^{25,52}, pharmacological inhibition of Cdk5/p25 activity is neuroprotective in vitro²⁸. Furthermore, conditional knockout of Cdk5 is neuroprotective in vivo^{23,28}. However, effective targeting of Cdk5 as a post-insult therapeutic approach has not been possible due to the lack of brain penetrant Cdk5/p25 inhibitors. Recently, we discovered a brain diffusible Cdk5 inhibitor (25–106) with exponential brain distribution kinetics and 30-fold greater specificity for Cdk5 over other cyclin dependent kinase family members⁵⁴. We hypothesized that this inhibitor could have rTBI therapeutic potential by blocking aberrant Cdk5/p25 activity. We first verified that this compound acted as a Cdk5 inhibitor in brain tissue by assessing the effect of slice treatment with 25–106 on phosphorylation of the Cdk5 reporter, Thr75 DARPP32 (Fig. 5B). Indeed, this site was strongly attenuated in brain slices by 25–106 treatment. Next, we assessed the neuroprotective capacity of 25–106 under excitotoxic conditions. The neuroprotective effect following Cdk5 inhibition was observed in ex vivo brain slices treated with high concentrations of NMDA/Gly as evidenced by TTC viability staining (Fig. 5C). These data confirm 25–106 as an inhibitor of Cdk5 in brain tissue and suggest it is neuroprotective in an ex vivo model of excitotoxicity.

To investigate the role of Cdk5/p25 signaling in rTBI, we assessed the excitotoxic activation of calpain following rTBI. As one index, we examined the breakdown of the calpain reporter, Fodrin into cleaved 150 and 120 kDa products 48 h post-injury⁵⁵. Rats subjected to rTBI displayed an increased activation of calpain protease (Fig. 5D). This effect corresponded to an increase in the aberrant activation of Cdk5 observed through the

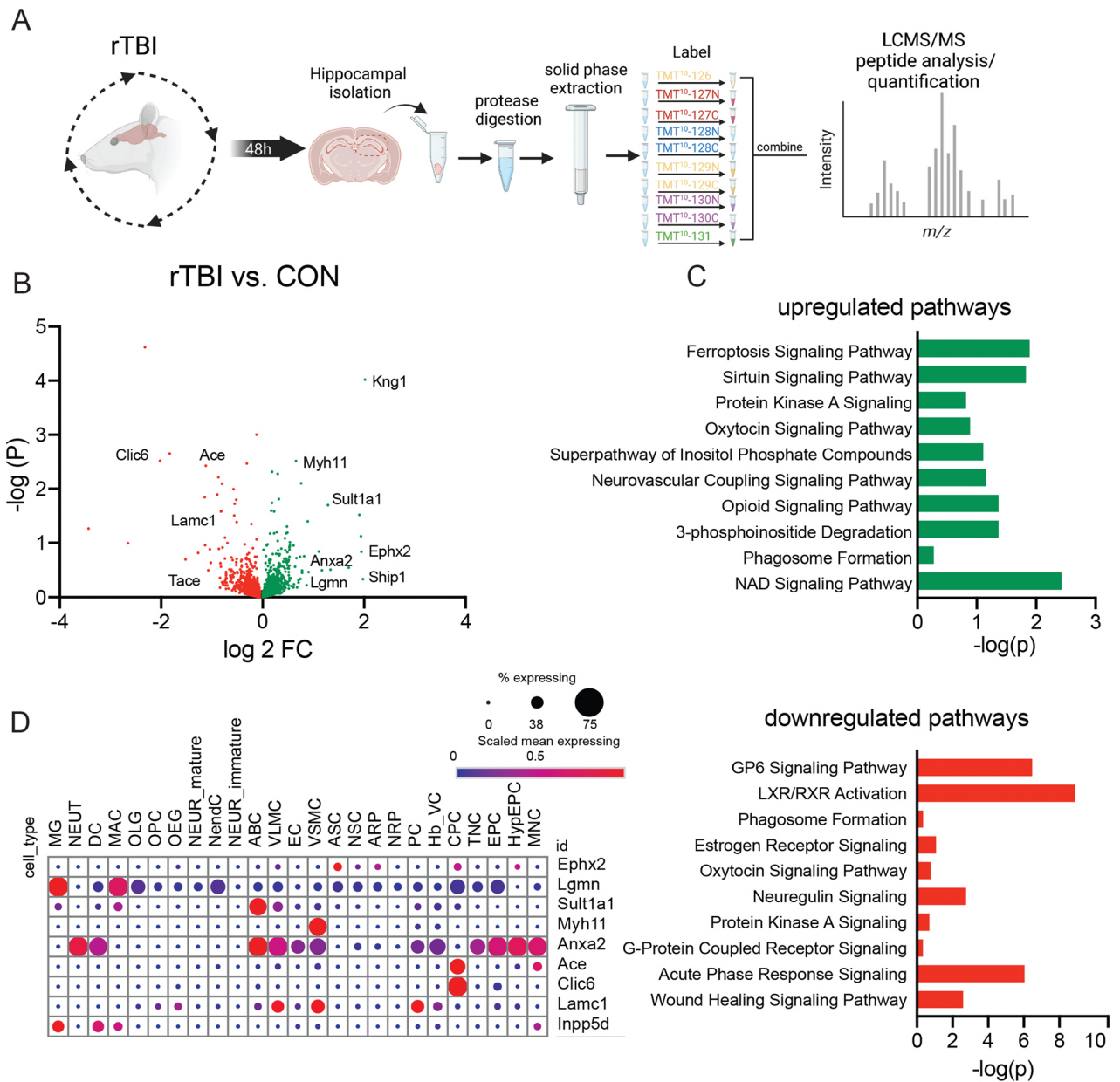
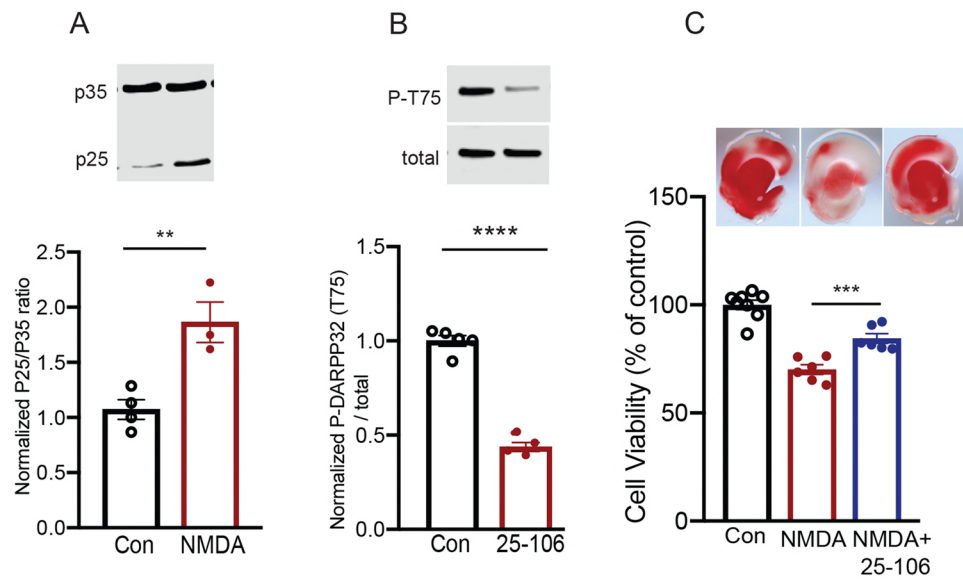


Figure 4. Proteomic alterations following rTBI. **(A)** Experimental design schematic for tissue isolation, extraction, labeling, and peptide detection for discovery proteomics. **(B)** Volcano plot of differentially expressed total proteins between rTBI and CON (control) rats (n = 5 pooled brains in duplicate per group, increased sites in green decreased sites in red). **(C)** (Top) Ingenuity Pathway Analysis of upregulated proteins following rTBI. (Bottom) Ingenuity Pathway Analysis of downregulated proteins following rTBI. **(D)** Cell-type expression profile in brain of differentially expressed proteins assessed from available dataset⁴⁷. Abbreviations: (ABC) Arachnoid barrier cells, (mNEUR) Mature neurons, (ARP) Astrocyte-restricted precursors, (NendC) Neuroendocrine cells, (ASC) Astrocytes, (NEUT) Neutrophils, (CPC) Choroid plexus epithelial cells, (NRP) Neuronal-restricted precursors, (DC) Dendritic cells, (NSC) Neural stem cells, (EC) Endothelial cells, (OEG) Olfactory ensheathing glia (EPC) Ependymocytes, (OLG) Oligodendrocytes, (Hb_VC) Hemoglobin-expressing vascular cells, (OPC) Oligodendrocyte precursor cells, (HypEPC) Hypendymal cells, (PC) Pericytes (ImmN) Immature neurons, (TNC) Tanycytes, (MAC) Macrophages, (VLNC) Vascular and leptomeningeal cells, (MG) Microglia, (VSMC) Vascular smooth muscle cells, (MNC) Monocytes.

production of the excitotoxic cofactor p25 (Fig. 5E). To assess the functionality of 25–106 in vivo, rats were treated with 50 mg/kg I.P. and brain lysates were blotted for Cdk5 dependent phosphorylation states. 25–106 caused a marked reduction in Cdk5 phosphorylation of Synapsin I 6 h after treatment in vivo (Fig. 5F). Together, these studies demonstrate aberrant activation of Cdk5 in excitotoxicity and rTBI and suggest 25–106 may be used as a therapeutic inhibitor of Cdk5.

ex vivo acute brain slices



In vivo hippocampal lysates

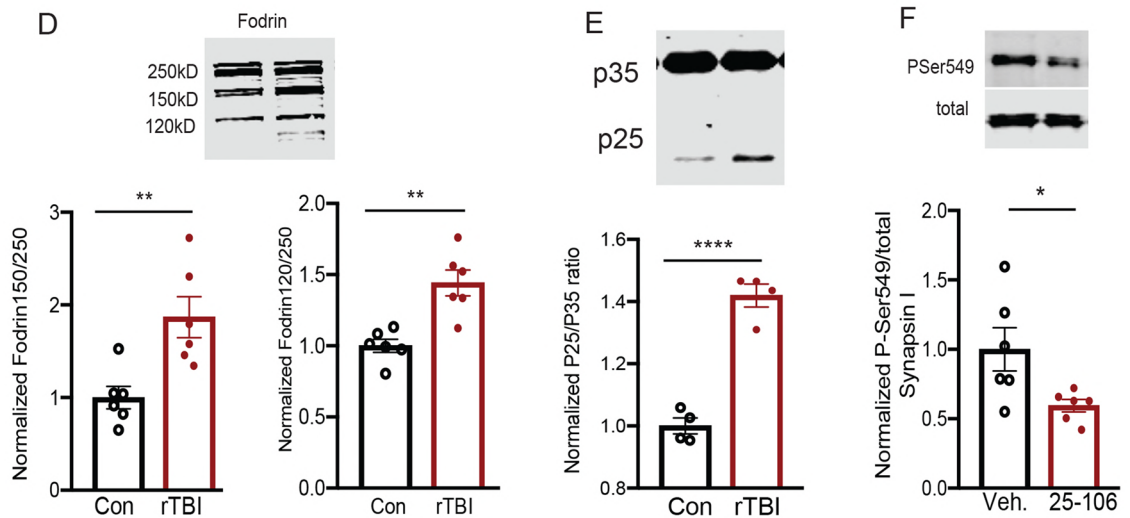


Figure 5. rTBI and excitotoxicity evoke aberrant Cdk5 activity and Cdk5 inhibition is protective. **(A)** Quantitative immunoblot analysis of acute brain slices for p35/25 after NMDA/Glycine (100/50 μ M, NMDA/Gly) treatment, ($n = 3-4$ per group) $p = 0.0081$ Student's t -test. **(B)** Quantitative immunoblot of acute brain slices for phospho-Thr75 DARPP32 after 1 h treatment 25-106 (10 μ M), ($n = 4-5$ per group) $p < 0.0001$ Student's t -test. **(C)** TTC viability staining of acute brain slices subjected to NMDA/Gly (100/50 μ M) treatment following preincubation with 25-106, ($n = 6-8$ per group) $F(2,17) = 45.19$ $p < 0.0001$ ANOVA (NMDA vs. NMDA + 25-106, $p = 0.0005$, Holm-Sidak post hoc). **(D)** Quantitative immunoblot of Fodrin breakdown products via calpain, $p = 0.0062$ (top), $p = 0.0014$ (bottom) Student's t -test ($n = 6$ per group). **(E)** Quantitative immunoblot of p25 generation following rTBI, ($n = 4$ per group) $p < 0.0001$ Student's t -test. **(F)** In vivo inhibition of Cdk5 assessed via quantitative immunoblot for P-Ser549/total Synapsin I after treatment with 50 mg/kg 25-106, ($n = 6$ per group) $p = 0.0305$ Student's t -test. All data are means \pm SEM, * $p < 0.05$, ** $p < 0.01$, *** $p < 0.001$, **** $p < 0.0001$. Full uncropped blots for each panel are provided in Supplemental Fig. 5.

Cdk5 enriched phosphoproteomics of injury. While conditional knockout of Cdk5 has shown its role in mediating various forms of neuronal injury and neurodegeneration, few Cdk5/p25 specific substrates and mechanisms have been identified. Utilizing this new inhibitor of Cdk5, we investigated the downstream effectors of Cdk5/p25 that may mediate neuronal demise and subsequent cognitive impairments associated with injury through Cdk5 phosphorylation site-directed phosphoproteomics of the hippocampus from control, rTBI, and rTBI rats treated with 25-106 (rTBI+25-106) 48 h post-injury, which corresponded to the generation of the

p25 fragment observed previously (Fig. 6A). For this proteomic analysis, mass spectrometry was conducted on lysates that have undergone an affinity enrichment with antibody-conjugated beads which binds peptides harboring proline-directed consensus phosphorylation sites including those commonly used by Cdk5⁵⁶. Robust changes in the Cdk5 phospho-landscape following rTBI and rTBI + treatment with 25–106 were apparent with 3,021 uniquely modified sites detected via LC/MS–MS (Fig. 6B–E). Rotational head trauma resulted in 653 upregulated phospho-sites with a fold change (FC) ≥ 1.3 (Fig. 6B), and a corresponding decrease in $650 \leq -1.3$ FC phospho-sites. Interestingly, differentially modified sites included alterations in the phosphorylation of proteins associated with AD such as Microtubule Associated Protein 2 (MAP2), and the Spinocerebellar Ataxia (SCA) associated protein, Diacylglycerol Lipase Alpha (DAGLA)^{57,58}. Additionally, the potential Cdk5-dependent phosphorylation states of proteins associated with cellular demise such as, apoptosis-stimulating protein of p53 (PPP1R13B), and homeostatic synaptic excitability such as GRIN2a (GluN2A) were altered by rTBI (Fig. 6B)^{59,60}.

We also observed a reciprocal relationship between the Cdk5 consensus site phospho-landscape of rTBI rats in comparison to rTBI rats treated with 25–106 (Fig. 6E, F), as many phospho-sites that were increased by rTBI were reduced in rTBI rats treated with 25–106. Specifically, of the 653 phospho-sites upregulated by rTBI, 473 of these sites were decreased in the hippocampus of rTBI rats treated with 25–106 representing an inverse relationship of 72.4% of the phospho-sites (Fig. 6F).

Ingenuity Pathway Analysis was used to identify key molecules and interacting pathways evoked by injury (Fig. 6G, H). Upregulated pathways from rTBI highlight molecules linked to neuronal impairments. These included altered phosphorylation states of molecules involved in Ca^{2+} signaling (Ca^{2+} Sig.), AMPK signaling (AMPK Sig.), GABA receptor signaling (GABAR Sig.), and protein ubiquitination (Pro. Ub.), as well as pathways invoked in neurodegeneration including amyotrophic lateral sclerosis signaling (ALS Sig.) and Huntington's disease signaling (HD Sig.) (Fig. 6G, top). Pathways assessed for proteins in which Cdk5-dependent phosphorylation states decreased following rTBI include glutamate receptor signaling (GluR Sig.), CREB signaling, reelin signaling, and synaptogenesis signaling pathways (SSP), all part of networks necessary for homeostatic neuronal function (Fig. 6G, bottom). Furthermore, the reduced phospho-states following rTBI evoked alterations in molecules associated with neuroinflammatory signaling (Neuroinflam Sig.) and neurovascular coupling signaling pathways (NVCSP) (Fig. 6G). Interestingly, rTBI rats treated with 25–106 (rTBI + 25,106) invoked phosphorylation state increases in pathways such as neurovascular coupling signaling pathway (NVCSP) and synaptogenesis signaling pathways (SSP), both of which displayed a reciprocal relationship in untreated rTBI rats (Fig. 6H). Rats subjected to rTBI + 25–106 also showed many phosphorylation state-dependent increases in proteins associated with inositol phosphate signaling including D-myo-inositol-5-phosphate metabolism (D-mIP5 met.), 3-phosphoinositide biosynthesis (3-PI Bs) and degradation (3-PI Deg.), as well as the super pathway of inositol phosphate compounds (SIPC) (Fig. 6H).

Additionally, we observed an inverse relationship in the pathways implicated in the phospho-sites that decreased following rTBI + 25–106. Here, we observed decreased phosphorylation of proteins associated with Huntington's disease signaling (HD Sig.), autophagy, and AMPK signaling, all of which were upregulated by rTBI alone (Fig. 6H). Also, rTBI + 25–106 decreased the phosphorylation states of molecules involved in 14–3–3 signaling including PPAR signaling, IL-15 production, reelin signaling, and SSP compared to TBI alone (Fig. 6H). Compared to controls, rTBI + 25–106 also evoked upregulation of PI3K/AKT, reelin, HIPPO, SSP, AMPK, 3-PI Deg, 3-PI biosynthesis (Bs), and SIPC signaling (Supplemental Fig. 3A). Additionally, compared to controls, rTBI + 25–106 caused downregulation of molecules involved in HIPPO, 14–3–3, GLUR, HD, G-protein coupled receptor, AMPK, Reelin, and SSP signaling (Supplemental Fig. 3B). Altogether, these data demonstrate the Cdk5/p25 signaling in the regulation of various neuronal pathways of injury involved in neuronal plasticity and synapse formation. Interestingly, this Cdk5 site enriched phosphoproteomic library derived from the acute phase of injury also unveiled the regulation of molecules implicated in chronic neurodegenerative conditions such as ALS and HD, two neurodegenerative conditions mediated via Cdk5^{61,62}.

As an indication of how the molecules with increased or decreased phosphorylation states alter the biological processes within cells, gene ontology analysis using the open-source platform, Enrichr was employed. The 10 most significant biological processes altered by increased phosphorylation states following rTBI include those highly specified in structural and axonal functions, such as the regulation of microtubule polymerization/depolymerization, axonogenesis, cell morphogenesis in neuronal differentiation, neuronal projection morphogenesis, regulation of supramolecular fiber organization, and cellular component assembly (Supplemental Fig. 3C). This pattern of effects on structural and axonal processes was also observed from gene ontology analysis of down-regulated phospho-sites following rTBI including regulation of microtubule polymerization/depolymerization, regulation of supramolecular fiber organization, axon development, cellular component assembly, and cell morphogenesis in neuron differentiation (Supplemental Fig. 3C).

Upregulated phospho-proteins in rats subjected to rTBI and rTBI + 25–106 also displayed similar patterns in the alterations of biological processes within structural and axonal gene ontologies including neuron projection morphogenesis, neuron projection development, cell morphogenesis/neuron differentiation, as well as regulation of microtubule polymerization/depolymerization, regulation of dendritic spine morphogenesis, and synapse organization (Supplemental Fig. 3D). Rats subjected to rTBI + 25–106 also showed decreased phosphorylation in proteins associated with regulation of microtubule polymerization/depolymerization, regulation of supramolecular fiber organization, axon development, axonogenesis, and cell morphogenesis in neuron differentiation relative to rTBI alone animals (Supplemental Fig. 3D). The same pattern of structural and axonal processes was further observed in ontological analysis of rTBI + 25–106 rat hippocampi as compared to controls (Supplement Fig. 3E).

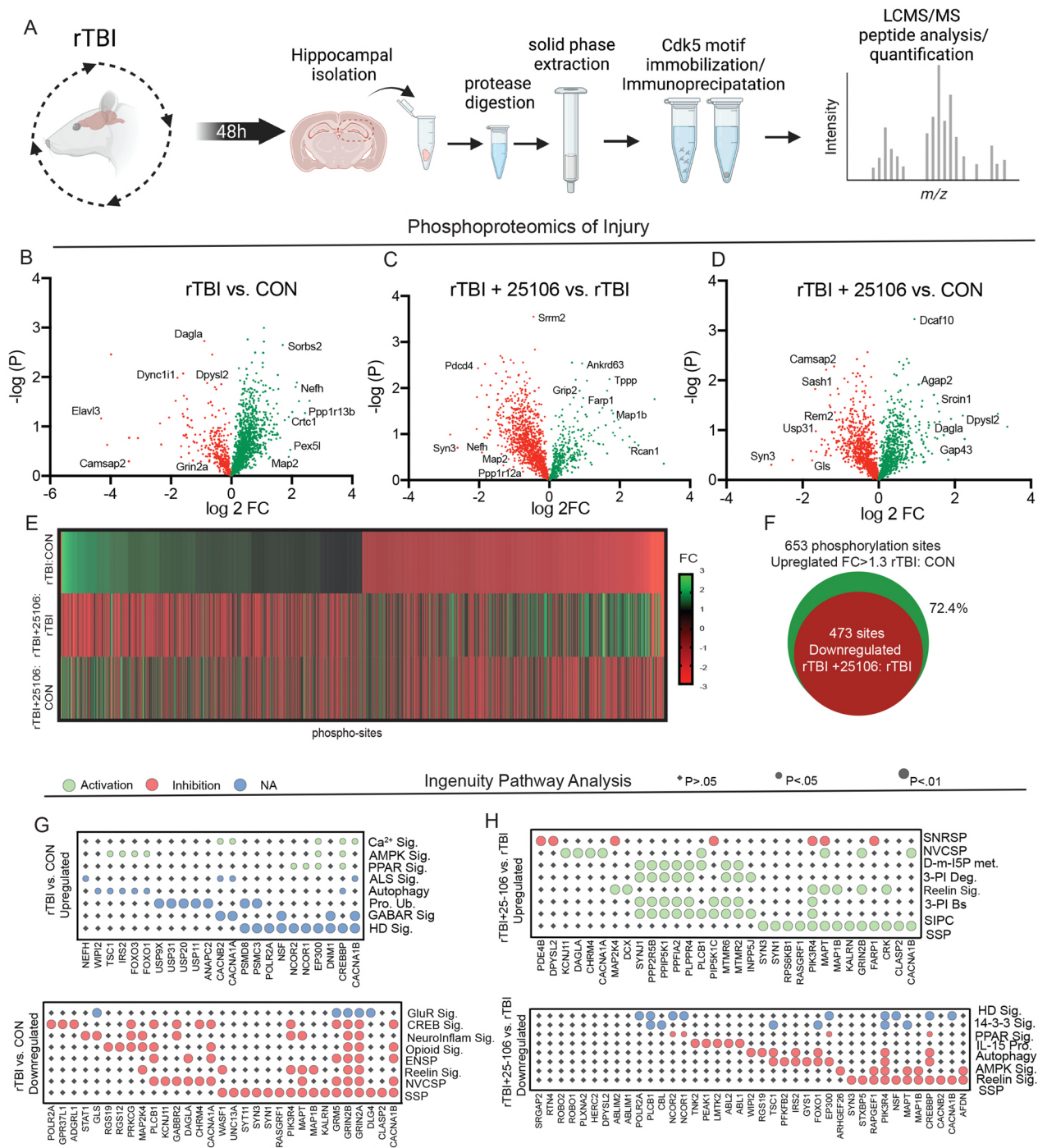


Figure 6. Cdk5 enriched phosphoproteomics of rTBI. **(A)** Experimental design schematic displaying tissue isolation, extraction, Cdk5 motif enrichment, and peptide detection and analysis. **(B)** Volcano plot of differentially phosphorylated proteins between rTBI and con rats. (n = 5 pooled brains in duplicate per group) (increased sites in green decreased sites in red). **(C)** Volcano plot of differentially phosphorylated proteins between rTBI + 25–106 and rTBI alone rats. **(D)** Volcano plot of differentially phosphorylated proteins between rTBI + 25–106 and con rats. **(E)** Heatmap of all differentially phosphorylated sites across three comparisons in B–D expressed by fold change of each phosphor-site. **(F)** Venn diagram representing overlapping sites with positive FC ≥ 1.3 in rTBI:CON and negative FC in rTBI + 25–106:rTBI. **(G)** Dot-plot display of Ingenuity Pathway Analysis of phosphoproteins and canonical pathways upregulated FC ≥ 1.3 by rTBI:Con (Top) and downregulated with a FC ≤ –1.3 by rTBI:Con (bottom). **(H)** Dot-plot display of Ingenuity Pathway Analysis of phosphoproteins and canonical pathways upregulated FC ≥ 1.3 by rTBI + 25,106:rTBI (Top) and downregulated with a FC ≤ –1.3 by rTBI + 25–106:rTBI (bottom).

Cdk5 inhibition is neuroprotective against rTBI. Conditional knockout of Cdk5 activity has been shown to provide neuroprotection from ischemia and experimental models of brain injury. However, the neuroprotective efficacy of pharmacological inhibition of Cdk5 remains unknown^{23,28}. To test the *in vivo* efficacy of 25–106, rats were subjected to rTBI and treated with 25–106 within 10 min after undergoing the injury procedure. Cognitive recovery was then assessed by fear conditioning 7 days post-injury (Fig. 7A, B). As previously observed, rats subjected to rTBI showed significant reductions in contextual fear learning and memory (freezing behavior). Also, treatment with 25–106 in the absence of rTBI had no effect on basal memory performance. In contrast, rTBI rats treated with 25–106 displayed no significant memory impairment in comparison to uninjured control animals and were significantly improved in mnemonic function compared to animals that received rTBI without Cdk5 inhibition (Fig. 7A). Similarly, rats subjected to rTBI alone showed significant reductions in

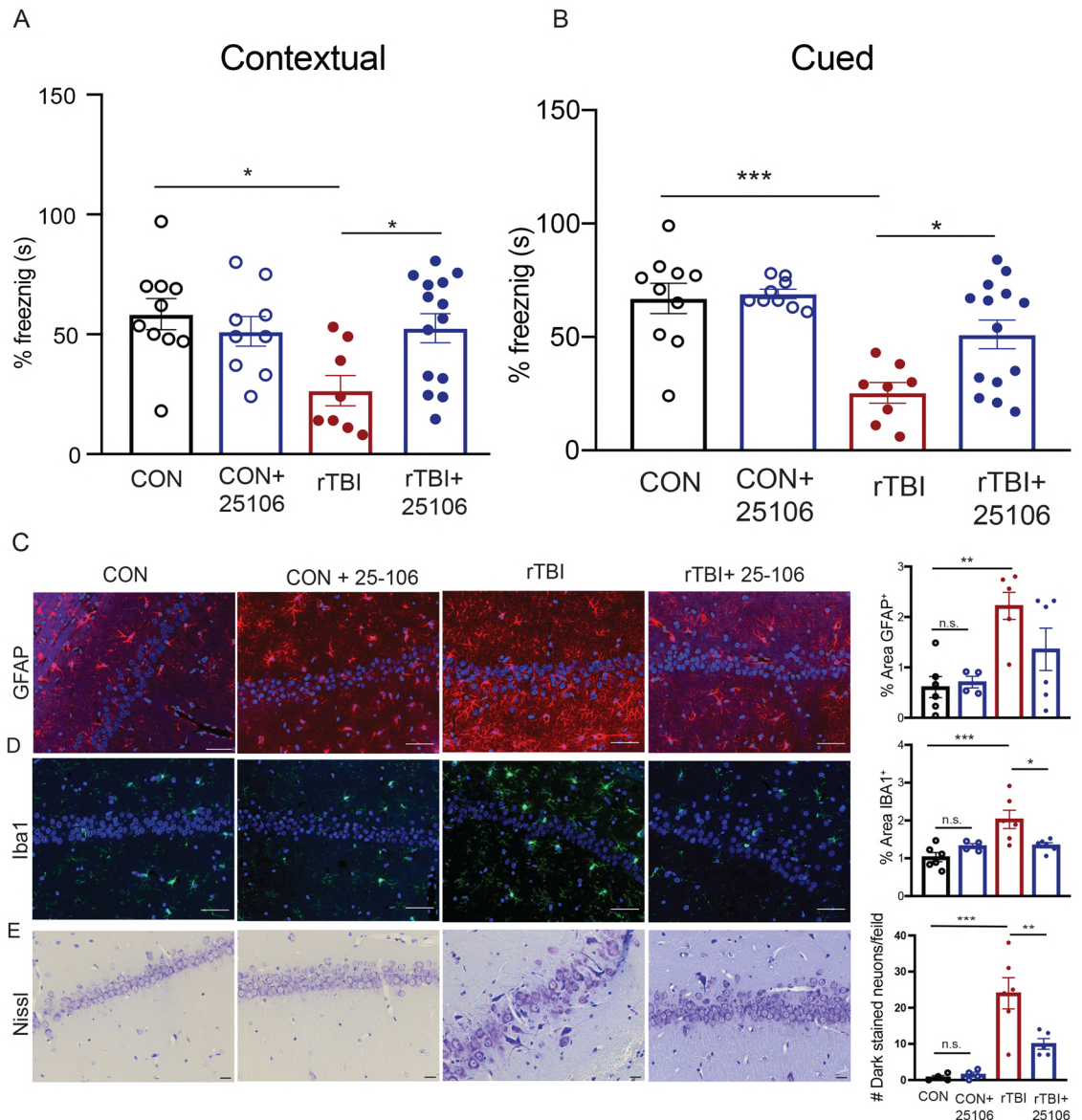


Figure 7. Cdk5 inhibition is neuroprotective against rTBI. **(A)** Fear conditioning freezing rates in contextual conditioning after rTBI treatment with 25–106 $F(3,37) = 4.057$, $p = 0.0137$, ANOVA; (Con-TBI $p = 0.0132$, TBI-TBI + 25,106, $p = 0.0384$ Holm-Sidak post hoc) ($n = 8–14$ per group). **(B)** Fear conditioning freezing rates in cued conditioning after rTBI treatment with 25–106 $F(3,37) = 10.07$, $p < 0.0001$ ANOVA; (Con-TBI $p = 0.0002$, TBI-TBI + 25,106 $p = 0.0137$ Holm-Sidak post hoc) ($n = 8–14$ per group). **(C)** Immunohistochemistry and quantitation of GFAP⁺ astrocytes in CA1 following rTBI and treatment with 25–106 $F(3,18) = 6.295$, $p = 0.0041$ ANOVA; (Con-TBI, $p = 0.0054$, Con-TBI + 25,106, $p = 0.2259$, Holm-Sidak post hoc) ($n = 4–6$ per group) Scale bars = 50 μm . **(D)** Immunohistochemistry and quantitation of IBA1⁺ microglia in CA1 following rTBI and treatment with 25–106 $F(3,18) = 8.070$, $p = 0.0013$ ANOVA; (Con-TBI, $p = 0.0009$, TBI-TBI + 25,106 $p = 0.0209$, Holm-Sidak post hoc) ($n = 4–6$ per group) Scale bars = 50 μm . **(E)** Nissl stained CA1 hippocampal subregion $F(3,15) = 14.70$ $p < 0.0001$ ANOVA (CON-TBI, $p = 0.0003$, TBI-TBI + 25–106 $p = 0.01$ Holm-Sidak post hoc) Scale bars 20 μm . All data are means \pm SEM, * $p < 0.05$, ** $p < 0.01$, *** $p < 0.001$.

cued fear learning and memory, while rTBI rats treated with 25–106 displayed cued-learning and memory rates similar to control animals and significantly improved from rTBI alone (Fig. 7B). Thus, acute post-injury Cdk5 inhibition almost completely blocked cognitive impairment in response to rTBI.

To assess the ability of 25–106 to ameliorate the neuropathological outcomes associated with impaired hippocampal memory, neuroinflammation was assessed via staining for astrogliosis and microgliosis 14 days post-injury (Fig. 7C, D). While rTBI animals alone showed the significant increases in CA1 astrocyte reactivity (GFAP⁺), 25–106 treatment attenuated this effect. Similarly, 25–106 prevented the neuroinflammatory activation of microglia in the hippocampus CA1 layers (Fig. 7D). In addition to these neuroprotective effects in the CA1 region, increases in gliosis occurred in other hippocampal layers including the dentate gyrus, and CA3 following rTBI and was attenuated by 25–106 (Supplemental Fig. 4A–F). In addition to inflammation, cell death is a major pathological change following TBI. To assess alterations in cell death, neurons displaying chromatolysis were counted. Consistent with other pathological outcomes, rTBI rats displayed an increase in damaged neurons following rTBI. Consistent with the other neuroprotective effects observed, this was ameliorated by treatment with 25–106 (Fig. 7E). Altogether, these data demonstrate the therapeutic potential of systemic Cdk5 inhibition via 25–106 to neuroprotect from rTBI.

Discussion

Rotational TBI remains the most clinically relevant form of brain trauma⁶³. However, understanding of these injuries has been, limited by the lack of rotational acceleration-induced injury models in rodents that accurately recapitulate patient phenotypes. Specifically, most preclinical rotational head trauma has been limited to large animal models due to the conserved gyrencephalic brain structures lacking in rodent models⁶⁴. While these large animal models of brain injury offer some physiologically relevant advantages, they remain costly and underpowered for genetic manipulations and preclinical screening of therapeutics⁶⁵. The fundamental challenge with rodent models of rTBI has been to scale rotational forces to small brain structures. Helmet telemetry data in humans have determined a typical sports-related head trauma induces rotational accelerations between 1 and 3 Krad/s^{230,66}. Scaling to the 2 g rat brain, these equate to rotational forces greater than 350 Krad/s^{231,67}.

Previously, rodent models including the Medical College of Wisconsin (MCW) and Closed-Head Impact Model of Engineered Rotational Acceleration (CHIMERA) have provided insights into modeling these injuries in small mammals. These models have demonstrated histopathological and behavioral abnormalities following injury and show differential outcomes in these injury models in comparison to blast models of TBI^{68–70}. However, these models have remained limited largely to initial characterizations and, in some instances, lack equivalent scalar angular forces. Here, we validate our rTBI model's rotational kinetics and demonstrate the feasibility for recapitulating numerous pathophysiological outcomes of head injuries across post-injury delays. Importantly, we have demonstrated several aspects of injury with this novel model of repetitive rTBI (summarized in Table 1). However, each of these outcomes depend upon various starting input conditions such as impact severity, animal age, anesthesia conditions, and post injury delay. Determining how each input variable effects the exact thresholds and temporal regulation of each pathological change observed here remains an important question.

Several animal studies indicate neuroinflammation as a key TBI consequence¹⁸. Depletion of infiltrating cells and halted neuroimmune responses improve behavioral and histological outcomes following cortical impact or fluid percussion injury in rodents^{78,79}. Similarly, we show our rTBI model induces diffuse neuroinflammation.

Post-injury delay	Outcome assessed	Conclusion	Relevance to other models
2 days	Neuroinflammation	rTBI rats show increased GFAP and IBA1 immunoreactivity in hippocampus	Acute inflammation ⁷¹
	Calpain activation	rTBI rats show calpain cleavage of p35 cofactor and Fodrin	Acute calpain activation in blast models ⁷²
	Axonal injury	rTBI rats show increased phosphorylated neurofilaments in the hippocampus.	Acute axonal damage p-NF ⁵⁰
	Proteomics	rTBI rats show global alterations in hippocampal proteomics	
	Phosphoproteomics	rTBI rats show dysregulation of Cdk5 phosphoproteomics	
7 days	Hippocampal electrophysiological axonal function	rTBI rats show impaired long-term potentiation (LTP)	Subacute Hippocampal axonal dysfunction ⁷³
	Memory	rTBI rats show decreased memory function in fear conditioning	Subacute Memory impairments following weight drop ⁷⁴
	Neuroinflammation	rTBI rats show increased TSPO PET/CT uptake across brain regions	Subacute neuroinflammation in FPI model ⁷⁵
14 days	Neuroinflammation	rTBI rats show increased GFAP and IBA1 immunoreactivity in hippocampus	Subacute neuroinflammation in "Run and Hit" model ⁷⁶
	Cell death	rTBI rats show increased cell death in the hippocampus	Subacute cell death in CCI ²³
6 months	Phospho-Tau (AT8) immunoreactivity	rTBI rats show increased AT8 immunoreactivity	AT8 immunoreactivity in human CTE patients ⁷⁷

Table 1. Summary of findings.

This inflammation is observed acutely (48 h) and persists into longer post-injury delay periods (7 and 14 d). We employed *in vivo* PET/CT imaging of TSPO as a potentially translational non-invasive diagnostic for rTBI. Increased TSPO expression likely indicates production of reactive oxygen species within neuroimmune cell populations such as microglia and astrocytes. This marker has been used clinically in patients with neurodegenerative conditions and in former professional football players exposed to chronic head injuries. The use of this marker as a diagnostic for acute brain injury in patients remains understudied^{32,34}. Interestingly, we observed no alteration in global brain uptake of TSPO, suggesting a mild or moderate neuroinflammatory phenotype. However, significant alterations in TSPO uptake were present when examining specific brain regions. The significance of region-specific neuroinflammatory responses such as these and the overall diagnostic sensitivity of this noninvasive technique patients with rTBI remains an important translational question.

Additionally, we observed the presence of increased hyperphosphorylated Tau in the form of AT8 immunoreactivity throughout the brains of rats subjected to rTBI 6 months post-injury. AT8 staining is specific for Tau that is abnormally phosphorylated at both Ser202 and Thr205, and the presence of AT8 Tau inclusions represents an underlying pathology in the post-mortem diagnosis of CTE³⁸. However, the preclinical understanding and development of CTE therapies remains limited by our abilities to model this disease preclinically. While some TBI models have shown acute increases in phosphorylated Tau, limited studies have demonstrated Tau inclusions and other CTE-like pathologies⁸⁰. In most studies, researchers have relied on overexpression of human isoforms of Tau and demonstrating an increased potential to aggregate following head trauma⁸⁰. While our finding here is exciting, more work will need to be conducted to determine the chronic effects of rTBI and the corresponding CTE-like pathologies including: the degree of TDP-43 pathology, stereological assessments of depleted neuronal populations, and solubility/isotypes of Tau inclusions. Notably, we did not observe increases in Tau phosphorylation at earlier stages of injury (14 days post-injury) via immunoblotting (data not shown). Assessing the temporal regulation of Tau phosphorylation remains an interesting question within this model and represents exciting potential for future research.

Brain injury results in a multitude of cognitive and behavioral impairments. Some of the most common symptoms reported by TBI survivors are persistent impairments in cognitive abilities including deficits in memory, attention, and executive functioning^{8,42}. These features are commonly linked to structural damage in the hippocampal formation following injury^{37,81}, and numerous animal models point to impaired hippocampal-mediated contextual and spatial memory impairments following TBI^{35,50,70}. In agreement, our rTBI model caused impaired hippocampal-dependent contextual fear memory and correlated with neuroinflammation in this region. Interestingly, amygdala-dependent cued fear memory was also impaired and exhibited a neuroinflammatory response. Structural damage to these areas, as well as brain-wide diffuse axonal injuries including interconnected efferent and afferent networks of the hippocampus/amygdala may be causally linked to these effects.

Underlying the observed memory impairment, rTBI caused an almost complete ablation of hippocampal long-term synaptic plasticity. This is consistent with the electrophysiological effects of other TBI models including fluid percussion, controlled cortical impact, and blast which also cause circuitry damage within the interconnected layers of the hippocampus^{82–84}. These alterations in hippocampal LTP occur in acute phases and persist into more chronic stages of TBI^{23,36,50,84}. However, the long-lasting effects of rTBI on LTP remain to be further characterized. While these alterations in axonal function likely link to axonal damage and structural changes in synaptic connections, assessing brain connectivity and structural alteration within axons remains an exciting question. TBI pathophysiology involves cellular depolarization, voltage-gated Ca²⁺ channel activation, massive glutamate release, and activation of Ca²⁺-dependent proteases such as calpain^{85,86}. Calpain represents a potential therapeutic target for TBI⁸⁷ and preclinical studies show promising calpain inhibitor neuroprotective activity^{88–91}. Cdk5/p25 activation is a principle downstream effector of excitotoxic calpain activation. Invocation of aberrant Cdk5 is broadly implicated in neuronal injury and neurodegeneration^{88–96}. Conditional knockout of Cdk5 is neuroprotective in models of ischemia and experimental brain injury^{23,28}. Transgenic overexpression of the aberrant co-activator of Cdk5, p25, induces rapid onset of AD in mice models⁵². Inhibition of p25 activity using small interfering peptides is neuroprotective in PD models⁹⁷. Therefore, aberrant Cdk5 activity represents a critical therapeutic target for acute injury and neurodegenerative conditions.

Given the potential efficacy of Cdk5 inhibition to block the deleterious behavioral and neuroinflammatory effects of rTBI, we used phosphoproteomics to enrich for phosphopeptides derived from potential Cdk5 substrates in the hippocampus. We report hundreds of novel potential Cdk5/p25 substrates phosphorylated in response rTBI but blocked when injury was followed by 25–106 treatment. Bioinformatic analysis implicated many of these in various cascades associated with cellular demise including AMPK, Ca²⁺, and neurodegenerative signaling. Importantly, human TBI survivors have a 56% increased risk of PD and a 2.3 times increased risk of developing AD^{21,98}. Since Cdk5/p25 activity is associated with the progression of both of these neurodegenerative conditions, it is likely that some of these substrates identified in the acute phases of rTBI likely contribute to longer lasting neuropathological effects of neurodegeneration. Understanding the dynamics of these phospho-substrates in the progression of TBI and as potential biomarkers of future brain degenerative conditions remains an exciting and expansive question generated by this work.

Several specific results within the global proteomic dataset derived here are also consistent with both preclinical models and clinical studies. For example, total proteome analysis in both rTBI and rTBI + 25–106 showed the highest upregulation of bradykinin family members Kng1 (FC = 4.0, rTBI FC = 6.6 rTBI + 25–106) and Kng2 (FC = 3.8, rTBI FC = 6.0 rTBI + 25–106). These proteins have been heavily implicated in animal TBI models as well as clinical studies⁹⁹. Kng1/Kng2 serve as ligands for B2 bradykinin receptors. In alignment with these targets as mediators of rTBI, B2 receptor antagonists have been tested in clinical trials for TBI treatment¹⁰⁰. We note that the induction of this inflammatory signaling cascade was not responsive to 25–106, and thus may exemplify mechanisms of injury that are not necessarily effectors of aberrant Cdk5 activation.

There is currently no approved treatment to ameliorate the neuropathological consequences of TBI. Having recently discovered the first brain-active systemic Cdk5 inhibitor, 25–106⁵⁴, we tested it here as a possible treatment for rTBI. While use of 25–106 in the acute phase of rTBI appears promising, injury delay periods to emergency room treatments can vary between patients and nearly 80% of TBI patients are initially treated and then released from emergency departments¹. The efficiency of Cdk5 inhibition in more sub-acute and chronic stages of rTBI remains to be explored. Current TBI patient treatments are directed at symptom management including anticonvulsants for seizures, diuretics to reduce pressure in the brain, and stimulants and anti-anxiety medications to increase alertness and reduce negative mood states^{101–104}. Clinical trials have investigated numerous possible neuroprotective interventions including NMDA antagonists to reduce excitotoxicity and anti-inflammatory agents but have not significantly improved outcomes^{100,105}. On the other hand, clotting agents such as tranexamic acid can prevent brain edema in the acute phase, although this treatment is limited to intracranial hemorrhages and may not be a useful approach for repetitive mild injuries mediated by axonal injury and inflammation¹⁰⁶. Altogether, this work brings forth a new model to the field of brain injury, assesses a novel neuroprotective treatment, and progresses our knowledge of the mechanisms mediating neuronal death caused by head trauma and other excitotoxic conditions.

Materials and methods

All methods were performed in accordance with relevant guidelines and regulations for safety and animal welfare of the University of Alabama at Birmingham (UAB) and approved by UAB. This study is in accordance with the ARRIVE guidelines.

Animals. Male Sprague Dawley rats (9–10 months old, Envigo) were used for all TBI experiments. All were single housed and maintained on a normal 12 h day/night cycle. For euthanasia in biochemical experiments, brains were collected via rapid live decapitation in the absence of anesthesia. For histological experiments, rats were euthanized via intraperitoneal injections of an anesthetic mixture of (100 mg/kg) ketamine (10 mg/kg) xylazine. For rTBI procedures, rats were maintained under anesthesia (isoflurane) at 1.5% for the duration of the procedure. All experiments were performed under approved protocols by the University of Alabama at Birmingham (UAB) Institutional Animal Care and Use Committees (IACUC).

Rotational traumatic brain injury (TBI) procedure. All rats were habituated to the room in which brain injuries occurred for 1 h, anesthetized using 1.5% isoflurane vapor, and sedation was maintained throughout the procedure via a nose-cone within the subject's helmet. Anesthetized rats were placed in a custom designed harness that was inserted into the base of the pendulum and locked tightly into place. The rat head was fitted into a freely rotational helmet with foam padding to secure head placement and rotation in one direction. Flowing N₂ gas was allowed to fill an Arduino controlled closed solenoid valve connected to an air motor and the pendulum was adjusted to a 90° angle raised approximately 84 cm from the base of the machine. Launch was electronically executed using custom software (LabVIEW) to open the solenoid allowing N₂ to propel the pendulum forward towards the ventral strike plate. Helmet impact results in a 90° rotation of the helmet and animal's head in both directions. Rotational forces were derived in LabVIEW from helmet velocity and exported into Excel. Each animal received 10 repetitive impact rotations over a 30 min period. Controls were maintained in the machine, under anesthesia for 30 min with no head rotation. Following injury each animal was assessed for normal locomotion and righting reflex abilities.

PET/CT imaging. Noninvasive positron emission tomography-computed tomography (PET/CT) imaging was conducted 7 days post TBI with [¹⁸F]DPA-714, a translocator protein (TSPO) radioligand produced at the Cyclotron Facility at the University of Alabama at Birmingham. Rats were injected with 300 µCi (11.1 MBq) of [¹⁸F]DPA-714 intravenously. Rats were immediately scanned using a GNEXT small animal PET/CT (Sofie Biosciences) for 30 min. Imaged regions of interests (ROIs) within the brain were drawn with CT guidance using VivoQuant (Invivo) and a 3D rat brain atlas (Allen brain atlas) was applied to automatically segment each brain region. The mean, maximum, hotspot, and heterogeneity of standard uptake values (SUVs) were determined using the formula: $SUV = [(MBq/mL) \times (animal\ wt.\ (g)) / injected\ dose\ (MBq)]$.

Histology. Histology was performed as described¹⁰⁷. Briefly, rats were transcardially perfused with 1X PBS/50 mM NaF followed by 10% formalin fixation. Brains were submerged in 10% formalin and fixed overnight, paraffin embedded and serially sectioned at 5 µm at Bregma level -3.3 to -4.5. Sections were deparaffinized in 100% xylene 3 × 5 min. Following deparaffination, slides were rehydrated using ethanol gradients of 5 min incubations in 100%EtOH, followed by 95%EtOH, and lastly 75%EtOH before being dipped in H₂O for 1 min. Following rehydration, slides were incubated in 1 × pre-warmed citrate antigen retrieval buffer (Thermo Fisher) and heated for 10 min in a pressure cooker followed by 20 min of cooling in the citrate buffer. Sections were then permeabilized and blocked in 0.03% Triton X-100/PBS containing 3% goat serum. DAB-stained sections underwent a 10 min incubation in 10% horseradish peroxidase. Immunohistochemistry was performed using glial fibrillary acidic protein (GFAP) (1:1000; Millipore) and ionized Ca²⁺-binding adapter protein (1:1000; Wako) incubated in 0.3% Tween 20/PBS overnight. Following 1 h of PBS washes, fluorescent visualization was performed using secondary antibodies Cy3 anti-rat (1:500), Alexa 488 anti-mouse (1:200) (Jackson Immuno) and imaged using an Olympus BX60 microscope mounted with Olympus DP74 digital camera. DAB-stained sections were incubated with anti-mouse biotin-conjugated secondary (1:500) or anti-rabbit biotin-conjugated secondary (1:500) (Jackson Immuno) followed by PBS washing and 30 min incubation with ready-to-use streptavidin peroxidase. DAB staining was performed using DAB substrate Kit (abcam) according to manufac-

turer's instructions and sections were incubated until brown precipitate was visible (5 min, AT8; 1 min SMI-31). Following DAB staining sections were incubated in hematoxylin counterstain and for 1 min, washed with H₂O, dehydrated in 100% EtOH (3 × 5 min) and cleared in xylene (3 × 5 min). For Nissl stains, paraffin embedded sections were deparaffinized and rehydrated in serial EtOH washes (as described above). Slides were then incubated in warmed (50 °C) 0.1% cresyl violet solution (Electron Microscopy Sciences) for 10 min. Following staining Nissl sections were differentiated in 95% EtOH, dehydrated in 100% EtOH, and cleared with 100% Xylene. All stains were performed using a minimum of 3 sections per animal and 4–6 animals per group. All stains within groups were analyzed using the same background thresholds (0–72; GFAP), (4–110; IBA1), and (72–234; AT8). Following thresholding, percent area of immunofluorescent positive staining was determined using ImageJ particle detection software (Fiji), optical density analysis of DAB stained sections was performed as described¹⁰⁸ and OD was determined by log (255/mean intensity) for 8bit images. Dark Nissl-stained neurons were detected using (Fiji) multipoint counting tool.

Ex vivo acute brain slice pharmacology. Brain slice pharmacology was performed as described⁵⁴. Briefly, brains were rapidly decapitated and submerged in ice cold Normal Krebs solution (125 mM NaCl, 2.5 mM KCl, 1.25 mM NaH₂PO₄, 25 mM NaHCO₃, 1.1 mM MgCl₂, 2 mM CaCl₂ and 25 mM glucose). Brains were coronally sectioned at 350 μm using a vibratome in regions of interest. Slices were recovered in oxygenated Krebs solution at 30 °C. Following recovery, slices were incubated in Krebs containing pharmacological interventions indicated of NMDA/Glycine (100 μM NMDA, 50 μM Gly, 1 h), 25–106 (10 μM, 1 h). Following treatment, slices were snap frozen in dry ice to terminate treatment. Following NMDA treatment, slices were incubated in 0.125% 2,3,5-Triphenyltetrazolium chloride (TTC) viability stain for 20 min. Stained slices were fixed in 4% PFA for 10 min and scanned. TTC viability was assessed by mean intensity of staining and expressed as percentage of control viability.

Immunoblotting. Immunoblotting was performed as previously described¹⁰⁷. Briefly, rat brains were rapidly dissected and submerged in a 4 °C solution of PBS/50 mM NaF. Subregions were dissected and snap frozen. Brain regions were subsequently homogenized in 1% SDS/50 mM NaF and sonicated at 40 dB pulses until tissue was completely homogenized. Protein concentrations were determined from lysates via BCA protein assay. Samples were diluted in 4 × lysis buffer and proteins were separated by molecular weight via SDS-PAGE. Proteins were then transferred to 0.45 nm nitrocellulose, blocked in Licor Blocking Buffer, and incubated with 1° antibody (Ab) overnight. Membranes were washed with 1 × TBS-T and incubated with Licor fluorescent 2° Ab for 1 h at room temperature. Proteins expression was visualized using Licor Odyssey CLx membrane scanner. Arbitrary units of florescent intensity for each protein band was quantified using ImageStudio. Phospho-band intensity was normalized to total protein bands, total protein bands were normalized to actin loading controls, and cleavage products were normalized to un-cleaved total protein. Antibodies used include p35/p25 (Cell Signaling Technology), phospho-Ser549 and total Synapsin I (PhosphoSolutions), Fodrin (Enzo Life Sciences), phospho-Thr75- and total DARPP32 (Cell Signaling Technology), EPHx2 (Abcam), Legumain (Cell Signaling), AT8 (Invitrogen), Actin (Invitrogen).

Neurophysiological recordings. Neurophysiological studies were conducted in rats 7 days post-injury as described⁵⁰. Briefly, brains were rapidly dissected in ice-cold artificial cerebrospinal fluid (ACSF; 75 mM sucrose, 87 mM NaCl, 2.5 mM KCl, 1.25 mM NaH₂PO₄, 25 mM NaHCO₃, 7 mM MgCl₂, 0.5 mM CaCl₂ and 10 mM glucose). Transverse hippocampal slices (350 μ) were sectioned using a vibratome (Leica Microsystems Inc., VT1000S) in NMDG cutting/recovery solution (N-methyl D-glucamine (100 mM), KCl (2.5 mM), NaH₂PO₄ (1.2 mM), NaHCO₃ (30 mM), HEPES (20 mM), MgSO₄ (1.0 mM), CaCl₂ (0.5 mM), and glucose (25 mM) at 30 °C (pH 7.3–7.4). After 2 min, slices were transferred to HEPES holding solution NaCl (92 mM), KCl (2.5 mM), NaH₂CO₃ (30 mM), NaH₂PO₄ (1 mM), HEPES (20 mM), D-Glucose (25 mM), MgCl₂ (1 mM), CaCl₂ (1 mM) for 1 h at 30 °C. Slices were allowed to incubate for 30 min in recording solution of oxygenated Krebs's (125 mM NaCl, 2.5 mM KCl, 1.25 mM NaH₂PO₄, 25 mM NaHCO₃, 1.1 mM MgCl₂, 2 mM CaCl₂ and 25 mM glucose) prior to recording.

Recordings were performed using a Multiclamp 700A amplifier with a Digidata 1322 and pClamp 10 software (Axon, Molecular devices, LLC). Field excitatory postsynaptic potentials (fEPSP) from CA1 were evoked by square current pulses (0.1 ms) at 0.033 Hz with a bipolar stimulation electrode (FHC, Bowdoinham, ME). Stimulus intensity was defined using a stimulus intensity required to induce 50% of the maximum EPSP slope using the input–output curves. The sample intensity was used for PPR recordings across different intervals. A stable baseline was recorded for at least 10 min prior to high frequency stimulation (HFS, 4 trains, 100 Hz, 1 s duration, separated by 20 s). Post-tetanic potentiation (PTP) was analyzed by taking the average of the slopes from the traces recorded during the first 2 min after HFS. LTP was assessed for at least 45–50 min following HFS. The PPR values were calculated by dividing the second fEPSP slope by the first fEPSP slope (fEPSP₂/fEPSP₁). All recordings were performed in the absence of any drug treatment and only 1 or 2 slices were recorded from each individual rat. Data were analyzed with Clampfit 10 software (Axon, Molecular devices, LLC).

Neurobehavior. Fear conditioning studies were performed as described¹⁰⁹. Briefly, rats were habituated to the behavioral room for 1 h before experimentation. Rats were placed in fear conditioning chambers (Med Associates) to establish baseline freezing rates between cohorts. The following day rats were subjected to fear conditioning training. Each rat was allowed to freely explore the chamber for 2 min followed by a 30 s tone terminating in a mild foot shock (0.7 mA). Rats remained in the chamber 2 min after shocking before returning to their home cage.

Context-dependent fear memory was assessed 24 h post-shock training. Rats were re-introduced into the conditioning box for 5 min. Freezing responses (motionless except respirations) were recorded using VideoFreeze software. Cued fear conditioning memory was assessed 27 h post-shock training where rats were allowed to explore a novel context with novel odor (vanilla). The rats were left exploring the novel context for 3 min without tone followed by a 3 min period with the training tone playing. Freezing responses (motionless except respirations) were recorded.

Shock sensitivity and nociceptive responses were assessed by returning rats to fear conditioning chambers and evaluating minimal thresholds to induce rat flinching, jumping, and vocalization of pain across adverse stimuli (0–1.5 mA) shocks.

Discovery proteomics. Freshly dissected and snap frozen rat hippocampi were sonicated, centrifuged, reduced with DTT, and alkylated with iodoacetamide. Total protein for each sample (10 mg) was trypsin digested, purified over C18 columns (Waters), enriched using the PTMScan Phospho CDK + CDK/MAPK Substrate Motif Antibodies (#9477/#2325 Cell Signaling Technology) and purified over C18 tips as previously described¹¹⁰. For total proteome analysis an additional 100 mg of each sample was digested with LysC and trypsin and digested samples were purified over C18 tips, labeled with TMT 10-plex reagent (Thermo), bRP fractionated (96 fractions concatenated non-sequentially to 12), and C18 purified for LC–MS/MS as previously described¹¹¹. LC–MS/MS analysis was performed using an Orbitrap-Fusion Lumos Tribrid mass spectrometer as described^{110,111} with replicate injections of each sample run non-sequentially for the phosphopeptide analysis. Briefly, peptides were separated using a 50 cm × 100 μM PicoFrit capillary column packed with C18 reversed-phase resin and eluted with a 90 min (Phospho) or 150 min (TMT total proteome) linear gradient of acetonitrile in 0.125% formic acid delivered at 280 nl/min. Full MS parameter settings are available upon request. MS spectra were evaluated by Cell Signaling Technology using Comet and the GFY-Core platform (Harvard University)^{112–114}. Searches were performed against the most recent update of the NCBI *Rattus norvegicus* database with a mass accuracy of ± 20 ppm for precursor ions and 0.02 Da product ions.

Results were filtered to a 1% peptide-level FDR with mass accuracy ± 5 ppm on precursor ions and presence of a phosphorylated residue for CDK Substrate enriched samples. TMT total proteome results were further filtered to a 1% protein level false discovery rate. Site localization confidence was determined using AScore¹¹⁵. All CDK Substrate quantitative results were generated using Skyline¹¹⁶ to extract the integrated peak area of the corresponding peptide assignments or in GFY-Core using signal: noise values for each peptide and summing individual signal: noise values for all peptides for a given protein for TMT total proteome data. Accuracy of quantitative data was ensured by manual review in Skyline or in the ion chromatogram files. Quantitative data was normalized across samples using median abundance for CDK Substrate data or sum signal: noise for TMT total proteome data.

Pathway and ontology analysis. Differentially modified phosphoproteins across all groups upregulated ≥ 1.3-fold change or downregulated ≤ -1.3 -fold change were subjected to Ingenuity Pathway Analysis (IPA), (Qiagen). Log-transformed p-values of significantly enriched canonical pathways and the phosphorylated/dephosphorylated molecules comprising each pathway were used to construct dot plots of canonical pathways significantly Up/downregulated in each condition. IPA Z-scores were used to predict activation or inhibition of each canonical pathway. Phosphoproteins exhibiting fold changes of greater ≥ 1.3 or ≤ -1.3 were subjected to gene ontology enrichment analysis via open source gene enrichment analysis software, Enrichr¹¹⁷. Biological processes and molecular functions from each gene list were derived based and the top 10 processes/functions were derived based on adjusted p-values.

Statistical analysis. Prior to analysis, all data was examined for normalcy using the Shapiro–Wilk test. In cases of parametric data with normal distributions of two group means Student's *t*-test were used. In cases of non-parametric comparison of means, the Mann–Whitney test was employed. When comparing more than two group means, one or two-way ANOVAs were used with Holm–Sidak post-hoc tests. When comparing two experimental variables within the same animal, Two-way repeated measures ANOVA was used. For all data, * = $p < 0.05$, ** = $p < 0.01$, *** = $p < 0.001$, **** = $p < 0.0001$. All statistical analysis was performed using Prism 6 (GraphPad Software, Inc.).

Data availability

All datasets used in this study are available from the corresponding author upon reasonable request.

Received: 27 September 2022; Accepted: 2 February 2023

Published online: 28 February 2023

References

- Capizzi, A., Woo, J. & Verduzco-Gutierrez, M. Traumatic brain injury: An overview of epidemiology, pathophysiology, and medical management. *Med. Clin.* **104**, 213–238. <https://doi.org/10.1016/j.mcna.2019.11.001> (2020).
- Guskiewicz, K. M. *et al.* Measurement of head impacts in collegiate football players: Relationship between head impact biomechanics and acute clinical outcome after concussion. *Neurosurgery* **61**, 1244–1252. <https://doi.org/10.1227/01.neu.0000306103.68635.1a> (2007)
- Mihalik, J. P., Bell, D. R., Marshall, S. W. & Guskiewicz, K. M. Measurement of head impacts in collegiate football players: An investigation of positional and event-type differences. *Neurosurgery* **61**, 1229–1235. <https://doi.org/10.1227/01.neu.0000306101.83882.c8> (2007)

4. Zhang, L., Yang, K. H. & King, A. I. Biomechanics of neurotrauma. *Neurol. Res.* **23**, 144–156. <https://doi.org/10.1179/016164101101198488> (2001).
5. McKee, A. C. & Daneshvar, D. H. The neuropathology of traumatic brain injury. *Handb. Clin. Neurol.* **127**, 45–66. <https://doi.org/10.1016/B978-0-444-52892-6.00004-0> (2015).
6. Riggio, S. & Wong, M. Neurobehavioral sequelae of traumatic brain injury. *Mt. Sinai J. Med.* **76**, 163–172. <https://doi.org/10.1002/msj.20097> (2009).
7. Pavlovic, D., Pekic, S., Stojanovic, M. & Popovic, V. Traumatic brain injury: Neuropathological, neurocognitive and neurobehavioral sequelae. *Pituitary* **22**, 270–282. <https://doi.org/10.1007/s11102-019-00957-9> (2019).
8. Arciniegas, D. B., Held, K. & Wagner, P. Cognitive impairment following traumatic brain injury. *Curr. Treat. Options Neurol.* **4**, 43–57. <https://doi.org/10.1007/s11940-002-0004-6> (2002).
9. Cuthbert, J. P. *et al.* Epidemiology of adults receiving acute inpatient rehabilitation for a primary diagnosis of traumatic brain injury in the United States. *J. Head Trauma Rehabil.* **30**, 122–135. <https://doi.org/10.1097/HTR.000000000000012> (2015).
10. Adams, J. W. *et al.* Lewy body pathology and chronic traumatic encephalopathy associated with contact sports. *J. Neuropathol. Exp. Neurol.* **77**, 757–768. <https://doi.org/10.1093/jnen/nly065> (2018).
11. Nortje, J. & Menon, D. K. Traumatic brain injury: Physiology, mechanisms, and outcome. *Curr. Opin. Neurol.* **17**, 711–718 (2004).
12. Masel, B. E. & DeWitt, D. S. Traumatic brain injury: A disease process, not an event. *J. Neurotrauma* **27**, 1529–1540. <https://doi.org/10.1089/neu.2010.1358> (2010).
13. Davis, A. E. Mechanisms of traumatic brain injury: Biomechanical, structural and cellular considerations. *Crit. Care Nurs. Q.* **23**, 1–13 (2000).
14. Povlishock, J. T. & Christman, C. W. The pathobiology of traumatically induced axonal injury in animals and humans: A review of current thoughts. *J. Neurotrauma* **12**, 555–564 (1995).
15. Raghupathi, R. Cell death mechanisms following traumatic brain injury. *Brain Pathol.* **14**, 215–222 (2004).
16. Chen, Y. *et al.* Cutting to the pathophysiology chase: Translating cutting-edge neuroscience to rehabilitation practice in sports-related concussion management. *J. Orthop. Sports Phys. Ther.* **49**, 811–818. <https://doi.org/10.2519/jospt.2019.8884> (2019).
17. Greve, M. W. & Zink, B. J. Pathophysiology of traumatic brain injury. *Mt. Sinai J. Med.* **76**, 97–104. <https://doi.org/10.1002/msj.20104> (2009).
18. Shi, K., Zhang, J., Dong, J. F. & Shi, F. D. Dissemination of brain inflammation in traumatic brain injury. *Cell Mol. Immunol.* **16**, 523–530. <https://doi.org/10.1038/s41423-019-0213-5> (2019).
19. Al-Dahhak, R., Khoury, R., Qazi, E. & Grossberg, G. T. Traumatic brain injury, chronic traumatic encephalopathy, and Alzheimer disease. *Clin. Geriatr. Med.* **34**, 617–635. <https://doi.org/10.1016/j.cger.2018.06.008> (2018).
20. Dams-O'Connor, K., Guetta, G., Hahn-Ketter, A. E. & Fedor, A. Traumatic brain injury as a risk factor for Alzheimer's disease: Current knowledge and future directions. *Neurodegener. Dis. Manag.* **6**, 417–429. <https://doi.org/10.2217/nmt-2016-0017> (2016).
21. Gardner, R. C. *et al.* Mild TBI and risk of Parkinson disease: A chronic effects of neurotrauma consortium study. *Neurology* **90**, e1771–e1779. <https://doi.org/10.1212/WNL.0000000000005522> (2018).
22. Iverson, G. L. *et al.* Chronic traumatic encephalopathy neuropathology might not be inexorably progressive or unique to repetitive neurotrauma. *Brain* **142**, 3672–3693. <https://doi.org/10.1093/brain/awz286> (2019).
23. Yousuf, M. A. *et al.* Involvement of aberrant cyclin-dependent kinase 5/p25 activity in experimental traumatic brain injury. *J. Neurochem.* **138**, 317–327. <https://doi.org/10.1111/jnc.13620> (2016).
24. Kusakawa, G. *et al.* Calpain-dependent proteolytic cleavage of the p35 cyclin-dependent kinase 5 activator to p25. *J. Biol. Chem.* **275**, 17166–17172. <https://doi.org/10.1074/jbc.M907757199> (2000).
25. Meyer, D. A. *et al.* Striatal dysregulation of Cdk5 alters locomotor responses to cocaine, motor learning, and dendritic morphology. *Proc. Natl. Acad. Sci. U. S. A.* **105**, 18561–18566. <https://doi.org/10.1073/pnas.0806078105> (2008).
26. Barnett, D. G. & Bibb, J. A. The role of Cdk5 in cognition and neuropsychiatric and neurological pathology. *Brain Res. Bull.* **85**, 9–13. <https://doi.org/10.1016/j.brainresbull.2010.11.016> (2011).
27. Torres-Altore, M. I. *et al.* Organophosphates dysregulate dopamine signaling, glutamatergic neurotransmission, and induce neuronal injury markers in striatum. *J. Neurochem.* **119**, 303–313. <https://doi.org/10.1111/j.1471-4159.2011.07428.x> (2011).
28. Meyer, D. A. *et al.* Ischemic stroke injury is mediated by aberrant Cdk5. *J. Neurosci.* **34**, 8259–8267. <https://doi.org/10.1523/JNEUROSCI.4368-13.2014> (2014).
29. Camins, A., Verdaguier, E., Folch, J., Canudas, A. M. & Pallas, M. The role of CDK5/P25 formation/inhibition in neurodegeneration. *Drug News Perspect.* **19**, 453–460. <https://doi.org/10.1358/dnp.2006.19.8.1043961> (2006).
30. Rowson, S., Brolinson, G., Goforth, M., Dietter, D. & Duma, S. Linear and angular head acceleration measurements in collegiate football. *J. Biomech. Eng.* **131**, 061016. <https://doi.org/10.1115/1.3130454> (2009).
31. Viano, D. C., Hamberger, A., Bolouri, H. & Saljo, A. Concussion in professional football: Animal model of brain injury—part 15. *Neurosurgery* **64**, 1162–1173. <https://doi.org/10.1227/01.NEU.0000345863.99099.C7> (2009) (**discussion** 1173).
32. Coughlin, J. M. *et al.* Neuroinflammation and brain atrophy in former NFL players: An in vivo multimodal imaging pilot study. *Neurobiol. Dis.* **74**, 58–65. <https://doi.org/10.1016/j.nbd.2014.10.019> (2015).
33. Israel, I. *et al.* Combined [(18)F]DPA-714 micro-positron emission tomography and autoradiography imaging of microglia activation after closed head injury in mice. *J. Neuroinflammation* **13**, 140. <https://doi.org/10.1186/s12974-016-0604-9> (2016).
34. Werry, E. L. *et al.* Recent developments in TSPO PET imaging as a biomarker of neuroinflammation in neurodegenerative disorders. *Int. J. Mol. Sci.* <https://doi.org/10.3390/ijms20133161> (2019).
35. Arulsamy, A., Teng, J., Colton, H., Corrigan, F. & Collins-Praino, L. Evaluation of early chronic functional outcomes and their relationship to pre-frontal cortex and hippocampal pathology following moderate-severe traumatic brain injury. *Behav. Brain Res.* **348**, 127–138. <https://doi.org/10.1016/j.bbr.2018.04.009> (2018).
36. Atkins, C. M. Decoding hippocampal signaling deficits after traumatic brain injury. *Transl. Stroke Res.* **2**, 546–555. <https://doi.org/10.1007/s12975-011-0123-z> (2011).
37. Bigler, E. D., Anderson, C. V. & Blatter, D. D. Temporal lobe morphology in normal aging and traumatic brain injury. *AJNR Am. J. Neuroradiol.* **23**, 255–266 (2002).
38. Lakis, N., Corona, R. J., Toshkezi, G. & Chin, L. S. Chronic traumatic encephalopathy—neuropathology in athletes and war veterans. *Neurol. Res.* **35**, 290–299. <https://doi.org/10.1179/1743132813Y.0000000177> (2013).
39. Johnson, V. E., Stewart, W. & Smith, D. H. Axonal pathology in traumatic brain injury. *Exp. Neurol.* **246**, 35–43. <https://doi.org/10.1016/j.expneurol.2012.01.013> (2013).
40. Anderson, K. J. *et al.* The phosphorylated axonal form of the neurofilament subunit NF-H (pNF-H) as a blood biomarker of traumatic brain injury. *J. Neurotrauma* **25**, 1079–1085. <https://doi.org/10.1089/neu.2007.0488> (2008).
41. Rabinowitz, A. R. & Levin, H. S. Cognitive sequelae of traumatic brain injury. *Psychiatr. Clin* **37**, 1–11. <https://doi.org/10.1016/j.psc.2013.11.004> (2014).
42. Mathias, J. L. & Mansfield, K. M. Prospective and declarative memory problems following moderate and severe traumatic brain injury. *Brain Inj.* **19**, 271–282. <https://doi.org/10.1080/02699050400005028> (2005).
43. Kenny, E. M. *et al.* Ferroptosis contributes to neuronal death and functional outcome after traumatic brain injury. *Crit. Care Med.* **47**, 410–418. <https://doi.org/10.1097/CCM.0000000000003555> (2019).
44. Yu, F. *et al.* Phagocytic microglia and macrophages in brain injury and repair. *CNS Neurosci. Ther.* **28**, 1279–1293. <https://doi.org/10.1111/cns.13899> (2022).

45. McKay, E. C. & Counts, S. E. Oxytocin receptor signaling in vascular function and stroke. *Front. Neurosci.* **14**, 574499. <https://doi.org/10.3389/fnins.2020.574499> (2020).
46. Ponsaerts, L. *et al.* Neuroinflammation in ischemic stroke: Inhibition of cAMP-specific phosphodiesterases (PDEs) to the rescue. *Biomedicines* <https://doi.org/10.3390/biomedicines9070703> (2021).
47. Ximerakis, M. *et al.* Single-cell transcriptomic profiling of the aging mouse brain. *Nat. Neurosci.* **22**, 1696–1708. <https://doi.org/10.1038/s41593-019-0491-3> (2019).
48. Baracaldo-Santamaria, D. *et al.* Revisiting excitotoxicity in traumatic brain injury: From bench to bedside. *Pharmaceutics* <https://doi.org/10.3390/pharmaceutics14010152> (2022).
49. Blennow, K., Hardy, J. & Zetterberg, H. The neuropathology and neurobiology of traumatic brain injury. *Neuron* **76**, 886–899. <https://doi.org/10.1016/j.neuron.2012.11.021> (2012).
50. Hernandez, A. *et al.* Exposure to mild blast forces induces neuropathological effects, neurophysiological deficits and biochemical changes. *Mol. Brain* **11**, 64. <https://doi.org/10.1186/s13041-018-0408-1> (2018).
51. Patrick, G. N. *et al.* Conversion of p35 to p25 deregulates Cdk5 activity and promotes neurodegeneration. *Nature* **402**, 615–622. <https://doi.org/10.1038/45159> (1999).
52. Cruz, J. C., Tseng, H. C., Goldman, J. A., Shih, H. & Tsai, L. H. Aberrant Cdk5 activation by p25 triggers pathological events leading to neurodegeneration and neurofibrillary tangles. *Neuron* **40**, 471–483 (2003).
53. Pao, P. C. & Tsai, L. H. Three decades of Cdk5. *J. Biomed. Sci.* **28**, 79. <https://doi.org/10.1186/s12929-021-00774-y> (2021).
54. Umfress, A. *et al.* Systemic administration of a brain permeable Cdk5 inhibitor alters neurobehavior. *Front. Pharmacol.* **13**, 863762. <https://doi.org/10.3389/fphar.2022.863762> (2022).
55. Czogalla, A. & Sikorski, A. F. Spectrin and calpain: A “target” and a “sniper” in the pathology of neuronal cells. *Cell Mol. Life Sci.* **62**, 1913–1924. <https://doi.org/10.1007/s00018-005-5097-0> (2005).
56. Carter, A. M. *et al.* Phosphoprotein-based biomarkers as predictors for cancer therapy. *Proc. Natl. Acad. Sci. U. S. A.* **117**, 18401–18411. <https://doi.org/10.1073/pnas.2010103117> (2020).
57. Iqbal, K. *et al.* Tau pathology in Alzheimer disease and other tauopathies. *Biochim. Biophys. Acta* **1739**, 198–210. <https://doi.org/10.1016/j.bbadis.2004.09.008> (2005).
58. Carlson, K. M., Andresen, J. M. & Orr, H. T. Emerging pathogenic pathways in the spinocerebellar ataxias. *Curr. Opin. Genet. Dev.* **19**, 247–253. <https://doi.org/10.1016/j.gde.2009.02.009> (2009).
59. Samuels-Lev, Y. *et al.* ASPP proteins specifically stimulate the apoptotic function of p53. *Mol. Cell* **8**, 781–794. [https://doi.org/10.1016/s1097-2765\(01\)00367-7](https://doi.org/10.1016/s1097-2765(01)00367-7) (2001).
60. Yong, X. L. H. *et al.* Regulation of NMDA receptor trafficking and gating by activity-dependent CaMKIIalpha phosphorylation of the GluN2A subunit. *Cell Rep.* **36**, 109338. <https://doi.org/10.1016/j.celrep.2021.109338> (2021).
61. Nguyen, M. D., Lariviere, R. C. & Julien, J. P. Deregulation of Cdk5 in a mouse model of ALS: Toxicity alleviated by perikaryal neurofilament inclusions. *Neuron* **30**, 135–147. [https://doi.org/10.1016/s0896-6273\(01\)00268-9](https://doi.org/10.1016/s0896-6273(01)00268-9) (2001).
62. Alvarez-Periel, E. *et al.* Cdk5 contributes to Huntington's disease learning and memory deficits via modulation of brain region-specific substrates. *Mol. Neurobiol.* **55**, 6250–6268. <https://doi.org/10.1007/s12035-017-0828-4> (2018).
63. Kleiven, S. Why most traumatic brain injuries are not caused by linear acceleration but skull fractures are. *Front. Bioeng. Biotechnol.* **1**, 15. <https://doi.org/10.3389/fbioe.2013.00015> (2013).
64. Armstead, W. M. & Vavilala, M. S. Improving understanding and outcomes of traumatic brain injury using bidirectional translational research. *J. Neurotrauma* **37**, 2372–2380. <https://doi.org/10.1089/neu.2018.6119> (2020).
65. Sorby-Adams, A. J., Vink, R. & Turner, R. J. Large animal models of stroke and traumatic brain injury as translational tools. *Am. J. Physiol. Regul. Integr. Comp. Physiol.* **315**, R165–R190. <https://doi.org/10.1152/ajpregu.00163.2017> (2018).
66. Rowson, S. *et al.* Rotational head kinematics in football impacts: An injury risk function for concussion. *Ann. Biomed. Eng.* **40**, 1–13. <https://doi.org/10.1007/s10439-011-0392-4> (2012).
67. Gennarelli, T. A. *et al.* Diffuse axonal injury and traumatic coma in the primate. *Ann. Neurol.* **12**, 564–574. <https://doi.org/10.1002/ana.410120611> (1982).
68. Stemper, B. D. *et al.* Behavioral outcomes differ between rotational acceleration and blast mechanisms of mild traumatic brain injury. *Front. Neurol.* **7**, 31. <https://doi.org/10.3389/fneur.2016.00031> (2016).
69. Namjoshi, D. R. *et al.* Merging pathology with biomechanics using CHIMERA (Closed-Head Impact Model of Engineered Rotational Acceleration): A novel, surgery-free model of traumatic brain injury. *Mol. Neurodegener.* **9**, 55. <https://doi.org/10.1186/1750-1326-9-55> (2014).
70. Sauerbeck, A. D. *et al.* modCHIMERA: A novel murine closed-head model of moderate traumatic brain injury. *Sci. Rep.* **8**, 7677. <https://doi.org/10.1038/s41598-018-25737-6> (2018).
71. Bolton, A. N. & Saatman, K. E. Regional neurodegeneration and gliosis are amplified by mild traumatic brain injury repeated at 24-hour intervals. *J. Neuropathol. Exp. Neurol.* **73**, 933–947. <https://doi.org/10.1097/NEN.000000000000115> (2014).
72. Wang, Y. *et al.* Calpain-2 as a therapeutic target in repeated concussion-induced neuropathy and behavioral impairment. *Sci. Adv.* <https://doi.org/10.1126/sciadv.aba5547> (2020).
73. Zhang, B. L. *et al.* Traumatic brain injury impairs synaptic plasticity in hippocampus in rats. *Chin. Med. J.* **124**, 740–745 (2011).
74. Luo, Y. *et al.* Mild traumatic brain injury induces memory deficits with alteration of gene expression profile. *Sci. Rep.* **7**, 10846. <https://doi.org/10.1038/s41598-017-11458-9> (2017).
75. Mayeux, J. P., Teng, S. X., Katz, P. S., Gilpin, N. W. & Molina, P. E. Traumatic brain injury induces neuroinflammation and neuronal degeneration that is associated with escalated alcohol self-administration in rats. *Behav. Brain Res.* **279**, 22–30. <https://doi.org/10.1016/j.bbr.2014.10.053> (2015).
76. Bolte, A. C. *et al.* Meningeal lymphatic dysfunction exacerbates traumatic brain injury pathogenesis. *Nat. Commun.* **11**, 4524. <https://doi.org/10.1038/s41467-020-18113-4> (2020).
77. Lakhan, S. E. & Kirchgessner, A. Chronic traumatic encephalopathy: the dangers of getting “dinged”. *Springerplus* **1**, 2. <https://doi.org/10.1186/2193-1801-1-2> (2012).
78. Willis, E. F. *et al.* Repopulating microglia promote brain repair in an IL-6-dependent manner. *Cell* **180**, 833–846. <https://doi.org/10.1016/j.cell.2020.02.013> (2020).
79. Witcher, K. G. *et al.* Traumatic brain injury causes chronic cortical inflammation and neuronal dysfunction mediated by microglia. *J. Neurosci.* **41**, 1597–1616. <https://doi.org/10.1523/JNEUROSCI.2469-20.2020> (2021).
80. Breen, P. W. & Krishnan, V. Recent preclinical insights into the treatment of chronic traumatic encephalopathy. *Front. Neurosci.* **14**, 616. <https://doi.org/10.3389/fnins.2020.00616> (2020).
81. Tomaiuolo, F. *et al.* Gross morphology and morphometric sequelae in the hippocampus, fornix, and corpus callosum of patients with severe non-missile traumatic brain injury without macroscopically detectable lesions: A T1 weighted MRI study. *J. Neurol. Neurosurg. Psychiatry* **75**, 1314–1322. <https://doi.org/10.1136/jnnp.2003.017046> (2004).
82. Goldstein, L. E. *et al.* Chronic traumatic encephalopathy in blast-exposed military veterans and a blast neurotrauma mouse model. *Sci. Transl. Med.* **4**, 134ra160. <https://doi.org/10.1126/scitranslmed.3003716> (2012).
83. Perez, E. J. *et al.* EphB3 signaling propagates synaptic dysfunction in the traumatic injured brain. *Neurobiol. Dis.* **94**, 73–84. <https://doi.org/10.1016/j.nbd.2016.06.007> (2016).
84. Titus, D. J. *et al.* Chronic cognitive dysfunction after traumatic brain injury is improved with a phosphodiesterase 4B inhibitor. *J. Neurosci.* **36**, 7095–7108. <https://doi.org/10.1523/JNEUROSCI.3212-15.2016> (2016).

85. Werner, C. & Engelhard, K. Pathophysiology of traumatic brain injury. *Br. J. Anaesth.* **99**, 4–9. <https://doi.org/10.1093/bja/aem131> (2007).
86. Lee, M. S. *et al.* Neurotoxicity induces cleavage of p35 to p25 by calpain. *Nature* **405**, 360–364. <https://doi.org/10.1038/35012636> (2000).
87. Saatman, K. E., Creed, J. & Raghupathi, R. Calpain as a therapeutic target in traumatic brain injury. *Neurotherapeutics* **7**, 31–42 (2010).
88. Buki, A., Farkas, O., Doczi, T. & Povlishock, J. T. Preinjury administration of the calpain inhibitor MDL-28170 attenuates traumatically induced axonal injury. *J. Neurotrauma* **20**, 261–268. <https://doi.org/10.1089/089771503321532842> (2003).
89. Czeiter, E. *et al.* Calpain inhibition reduces axolemmal leakage in traumatic axonal injury. *Molecules* **14**, 5115–5123. <https://doi.org/10.3390/molecules14125115> (2009).
90. Kawamura, M. *et al.* Calpain inhibitor MDL 28170 protects hypoxic-ischemic brain injury in neonatal rats by inhibition of both apoptosis and necrosis. *Brain Res.* **1037**, 59–69. <https://doi.org/10.1016/j.brainres.2004.12.050> (2005).
91. Meyer, D. *et al.* Ischemic stroke is mediated by aberrant Cdk5. *J. Neurosci.* **34**, 8259–8267 (2014).
92. Slevin, M. & Krupinski, J. Cyclin-dependent kinase-5 targeting for ischaemic stroke. *Curr. Opin. Pharmacol.* (2008).
93. Pozo, K. & Bibb, J. A. The emerging role of Cdk5 in cancer: A novel cancer therapy target. *Trends Cancer* **2**, 606–618 (2016).
94. Bk, B. *et al.* Overexpression of the Cdk5 inhibitory peptide in motor neurons rescues of amyotrophic lateral sclerosis phenotype in a mouse model. *Hum. Mol. Genet.* **28**, 3175–3187. <https://doi.org/10.1093/hmg/ddz118> (2019).
95. Tsai, L. H., Lee, M. S. & Cruz, J. Cdk5, a therapeutic target for Alzheimer's disease?. *Biochim. Biophys. Acta* **1697**, 137–142. <https://doi.org/10.1016/j.bbapap.2003.11.019> (2004).
96. Wei, F. Y. & Tomizawa, K. Cyclin-dependent kinase 5 (Cdk5): A potential therapeutic target for the treatment of neurodegenerative diseases and diabetes mellitus. *Mini Rev. Med. Chem.* **7**, 1070–1074. <https://doi.org/10.2174/138955707782110114> (2007).
97. Binukumar, B. K. *et al.* Peptide TFP5/TP5 derived from Cdk5 activator P35 provides neuroprotection in the MPTP model of Parkinson's disease. *Mol. Biol. Cell* **26**, 4478–4491. <https://doi.org/10.1091/mbc.E15-06-0415> (2015).
98. Plassman, B. L. *et al.* Documented head injury in early adulthood and risk of Alzheimer's disease and other dementias. *Neurology* **55**, 1158–1166. <https://doi.org/10.1212/wnl.55.8.1158> (2000).
99. Trabold, R. *et al.* The role of bradykinin B(1) and B(2) receptors for secondary brain damage after traumatic brain injury in mice. *J. Cereb. Blood Flow Metab.* **30**, 130–139. <https://doi.org/10.1038/jcbfm.2009.196> (2010).
100. Beauchamp, K., Mutlak, H., Smith, W. R., Shohami, E. & Stahel, P. F. Pharmacology of traumatic brain injury: Where is the “golden bullet”? *Mol. Med.* **14**, 731–740. <https://doi.org/10.2119/2008-00050.Beauchamp> (2008).
101. Kirmani, B. F., Robinson, D. M., Fonkem, E., Graf, K. & Huang, J. H. Role of anticonvulsants in the management of posttraumatic epilepsy. *Front. Neurol.* **7**, 32. <https://doi.org/10.3389/fneur.2016.00032> (2016).
102. Wakai, A., McCabe, A., Roberts, I. & Schierhout, G. Mannitol for acute traumatic brain injury. *Cochrane Database Syst. Rev.* <https://doi.org/10.1002/14651858.CD001049.pub5> (2013).
103. Levin, H. *et al.* Methyphenidate treatment of cognitive dysfunction in adults after mild to moderate traumatic brain injury: Rationale, efficacy, and neural mechanisms. *Front. Neurol.* **10**, 925. <https://doi.org/10.3389/fneur.2019.00925> (2019).
104. Silverberg, N. D. & Panenka, W. J. Antidepressants for depression after concussion and traumatic brain injury are still best practice. *BMC Psychiatry* **19**, 100. <https://doi.org/10.1186/s12888-019-2076-9> (2019).
105. Bergold, P. J. Treatment of traumatic brain injury with anti-inflammatory drugs. *Exp. Neurol.* **275**(Pt 3), 367–380. <https://doi.org/10.1016/j.expneurol.2015.05.024> (2016).
106. Cap, A. P. CRASH-3: A win for patients with traumatic brain injury. *Lancet* **394**, 1687–1688. [https://doi.org/10.1016/S0140-6736\(19\)32312-8](https://doi.org/10.1016/S0140-6736(19)32312-8) (2019).
107. Umfress, A. *et al.* Neuropathological effects of chemotherapeutic drugs. *ACS Chem. Neurosci.* **12**, 3038–3048. <https://doi.org/10.1021/acscchemneuro.1c00338> (2021).
108. Crowe, A. R. & Yue, W. Semi-quantitative determination of protein expression using immunohistochemistry staining and analysis: An integrated protocol. *Bio Protoc.* **9**, 100. <https://doi.org/10.21769/BioProtoc.3465> (2019).
109. Plattner, F. *et al.* The role of ventral striatal cAMP signaling in stress-induced behaviors. *Nat. Neurosci.* **18**, 1094–1100. <https://doi.org/10.1038/nn.4066> (2015).
110. Stokes, M. P. *et al.* Complementary PTM profiling of drug response in human gastric carcinoma by immunoaffinity and IMAC methods with total proteome analysis. *Proteomes* **3**, 160–183. <https://doi.org/10.3390/proteomes3030160> (2015).
111. Possemato, A. P. *et al.* Multiplexed phosphoproteomic profiling using titanium dioxide and immunoaffinity enrichments reveals complementary phosphorylation events. *J. Proteom. Res.* **16**, 1506–1514. <https://doi.org/10.1021/acs.jproteome.6b00905> (2017).
112. Eng, J. K., Jahan, T. A. & Hoopmann, M. R. Comet: An open-source MS/MS sequence database search tool. *Proteomics* **13**, 22–24. <https://doi.org/10.1002/pmic.201200439> (2013).
113. Huttlin, E. L. *et al.* A tissue-specific atlas of mouse protein phosphorylation and expression. *Cell* **143**, 1174–1189. <https://doi.org/10.1016/j.cell.2010.12.001> (2010).
114. Villen, J., Beausoleil, S. A., Gerber, S. A. & Gygi, S. P. Large-scale phosphorylation analysis of mouse liver. *Proc. Natl. Acad. Sci. U. S. A.* **104**, 1488–1493. <https://doi.org/10.1073/pnas.0609836104> (2007).
115. Beausoleil, S. A., Villen, J., Gerber, S. A., Rush, J. & Gygi, S. P. A probability-based approach for high-throughput protein phosphorylation analysis and site localization. *Nat. Biotechnol.* **24**, 1285–1292. <https://doi.org/10.1038/nbt1240> (2006).
116. MacLean, B. *et al.* Skyline: An open source document editor for creating and analyzing targeted proteomics experiments. *Bioinformatics* **26**, 966–968. <https://doi.org/10.1093/bioinformatics/btq054> (2010).
117. Chen, E. Y. *et al.* Enrichr: interactive and collaborative HTML5 gene list enrichment analysis tool. *BMC Bioinform.* **14**, 128. <https://doi.org/10.1186/1471-2105-14-128> (2013).

Acknowledgements

We thank the UAB Behavioral Assessment Core for assistance, and Carlo Wayan, Curtis Anderson, Jose Becerra, Stacy Donovan, and Athanasios Spiropoulos at UT Dallas Mechanical Engineering Senior Design Program. We thank Divya Shaw and the UT Arlington Mechanical and Aerospace Engineering Dept., and Naveen Varma and the UAB School of Engineering. We thank V. Yang for assistance with data library deposition. We thank the UAB Comprehensive Cancer Center's Preclinical Imaging Shared Facility (P30CA013148). We thank University of Texas Southwestern Dept of Psychiatry and Carol Tamminga for support of this work. We appreciate the IACUC staffs at UTSW and UAB for help in developing this model.

Author contributions

A.U., A.C., S.P.S.D., D.E., R.A., A.M., A.S., I.H., S.A., T.W., C.S., K.A., and M.S. conducted experiments, collected data, and performed formal analysis. H. Luo and H. Lu. engineered the model. S.S. and A.N. synthesized reagents. D.C., N.K., and S.M. conducted analysis and data visualization. A.U., C.R., J.A.B. conceived the study and experimental design. All authors contributed to editing and approval of the final manuscript.

Funding

This research was facilitated by NINDS T32 Predoctoral Training Fellowship (NS061788) (A.U.). Aspects were supported by pilot funding from the Yale NIDA Neuroproteomics Center (DA018343, A.C.), the DOE (DE-NA 0003962, H.L.) and the University of Texas Louis A. Beachel Jr. endowed Chair (H.L.). This work was also supported by UAB Radiology/CCTS Pilot Research Award. Model development was supported by the Texas Institute for Brain Injury and Repair. Aspects of this work were facilitated by NIH grants NS073855, MH116896, and MH126948 (J.A.B). Aspects of this work were also facilitated by an SDHB Pheo Para Coalition Investigator Award, and an NETRF Accelerator Award.

Competing interests

The authors declare no competing interests.

Additional information

Supplementary Information The online version contains supplementary material available at <https://doi.org/10.1038/s41598-023-29322-4>.

Correspondence and requests for materials should be addressed to J.A.B.

Reprints and permissions information is available at www.nature.com/reprints.

Publisher's note Springer Nature remains neutral with regard to jurisdictional claims in published maps and institutional affiliations.



Open Access This article is licensed under a Creative Commons Attribution 4.0 International License, which permits use, sharing, adaptation, distribution and reproduction in any medium or format, as long as you give appropriate credit to the original author(s) and the source, provide a link to the Creative Commons licence, and indicate if changes were made. The images or other third party material in this article are included in the article's Creative Commons licence, unless indicated otherwise in a credit line to the material. If material is not included in the article's Creative Commons licence and your intended use is not permitted by statutory regulation or exceeds the permitted use, you will need to obtain permission directly from the copyright holder. To view a copy of this licence, visit <http://creativecommons.org/licenses/by/4.0/>.

© The Author(s) 2023